GeoScienceWorld
Lithosphere
Volume 2021, Article ID 7866219, 25 pages
https://doi.org/10.2113/2021/7866219

Lithosphere

Research Article

Quantifying Normal Fault Evolution from River Profile Analysis in the Northern Basin and Range Province, Southwest Montana, USA

Ian P. Armstrong, Brian J. Yanites, Nate Mitchell, Clarke DeLisle, and Bruce J. Douglas

Indiana University, Earth and Atmospheric Sciences, 1001 East 10th St., Bloomington, IN 47405, USA

Correspondence should be addressed to Ian P. Armstrong; ianarmst@iu.edu

Received 16 September 2020; Accepted 5 February 2021; Published 19 April 2021

Academic Editor: Pierre Valla

Over the past few decades, tectonic geomorphology has been widely implemented to constrain spatial and temporal patterns of fault slip, especially where existing geologic or geodetic data are poor. We apply this practice along the eastern margin of Bull Mountain, Southwest Montana, where 15 transient channels are eroding into the flat, upstream relict landscape in response to an ongoing period of increased base level fall along the Western North Boulder fault. We aim to improve constraints on the spatial and temporal slip rates across the Western North Boulder fault zone by applying channel morphometrics, cosmogenic erosion rates, bedrock characteristics, and calibrated reproductions of the modern river profiles using a 1-dimensional stream power incision model that undergoes a change in the rate of base level fall. We perform over 10^4 base level fall simulations to explore a wide range of fault slip dynamics and stream power parameters. Our best fit simulations suggest that the Western North Boulder fault started as individual fault segments along the middle to southern regions of Bull Mountain that nucleated around 6.2 to 2.5 Ma, respectively. This was followed by the nucleation of fault segments in the northern region around 1.5 to 0.4 Ma. We recreate the evolution of the Western North Boulder fault to show that through time, these individual segments propagate at the fault tips and link together to span over 40 km, with a maximum slip of 462 m in the central portion of the fault. Fault slip rates range from 0.02 to 0.45 mm/yr along strike and are consistent with estimates for other active faults in the region. We find that the timing of fault initiation coincides well with the migration of the Yellowstone hotspot across the nearby Idaho-Montana border and thus attribute the initiation of extension to the crustal bulge from the migrating hotspot. Overall, we provide the first quantitative constraints on fault initiation and evolution of the Western North Boulder fault, perhaps the farthest north basin in the Northern Basin and Range province that such constraints exist. We show that river profiles are powerful tools for documenting the spatial and temporal patterns of normal fault evolution, especially where other geologic/geodetic methods are limited, proving to be a vital tool for accurate tectonic hazard assessments.

1. Introduction

The evolution of topography within mountainous landscapes is driven by the competition between two major processes: (1) the tectonic uplift of rock [1] and (2) climatically and lithologically controlled erosion [2–4]. When a tectonic perturbation like normal faulting causes a relative drop in the base level, relief is generated, and bedrock rivers respond by incising into the landscape undergoing relative uplift. The transition from the undisturbed upstream relict channel to the actively incising (transient) channel is signified by a discontinuity in the channel slope, known as a knickpoint or knickzone. The spatial distributions of knickpoints and their migration rates are strongly linked to rock uplift rates and therefore act as an archive of tectonic activity within a landscape [5–15].

In the past few decades, the widespread study and improvement of bedrock channel morphology analysis, cosmogenic nuclide dating, and river incision modeling techniques have produced insight into transient channel behavior. Combined with the increasing availability of high-resolution digital elevation models (DEMs), these advances have provided the data necessary to extract tectonic

information from topography around the globe [4]. For example, Ellis et al. [5] found that multiple series of knickpoints upstream of normal faults in the Pine Forest, Santa Rosa, and Jackson Ranges in Northwestern Nevada were attributed to ~220 m of base level drop since the Pliocene. Boulton and Whittaker [16] found that knickpoints upstream of normal faults in the Hatay Graben in southern Turkey were formed by a 5-fold acceleration in slip rates, and that the half-graben is now bounded by a soft-linked normal fault, proving to have substantial hazard implications for the region. Furthermore, Gallen and Wegmann [17] found that the spatial and temporal changes in bedrock channel steepness (k_{sn}) are consistent with the growth and linkage of the large Ptolemy and South-Central Crete normal fault systems, validating the findings of numerous other studies that show that river profiles will adjust their steepness to keep pace with the rate of rock uplift [13, 18–20]. These studies are just a few of many demonstrating that bedrock channel analyses successfully provide insights into the relative magnitude and timing of tectonic perturbations, even where existing geologic/geodetic constraints are poor [4, 5, 9–11, 14, 15, 17, 20–24].

Despite the growing amount of literature using this emerging approach, few studies on the detailed evolution of individual normal fault systems, particularly in the northern end of the Basin and Range province, Southwest Montana, exist. This is due to the fact that the relatively young, slow moving normal fault systems in this region are often inadequately constrained with conventional techniques like thermochronology, which require large amounts of fault throw to exhume thermally reset minerals [25], or with geodetics, which require relatively rapid fault slip rates [26]. Furthermore, thermochronology and geodetics have temporal resolutions of 10^6-10^7 and 10^0-10^1 years, respectively, hindering the ability to constrain fault slip at the critical time scales of $>10^5$-10^6 years. However, by analyzing bedrock channel morphology and applying stream power incision models [1, 10, 11, 27–29], transient landscapes offer an excellent opportunity to constrain the timing and pattern of base level fall along young fault systems with low slip rates and total throw, even when other geomorphic or geodetic data is lacking [16].

This paper aims to use bedrock channel analysis to place constraints on the spatial and temporal slip rates across the Western North Boulder normal fault in the northern end of the Basin and Range province, Southwest Montana (Figures 1(a)–1(c)). Fault slip data in this low strain rate, seismically active region, are sparse and/or poorly constrained, limiting confidence in seismic hazard assessments [30]. Furthermore, the young, actively extending Western North Boulder fault has relatively little fault throw (Johns et al., 1982; Stickney and Bartholomew, 1987), providing an opportunity to observe the beginning/intermediate phases of normal fault evolution and how the surrounding landscape responds in such a scenario. Normal fault mechanics predict elliptical patterns of slip along strike with higher slip rates along the central portion of the fault relative to the distal portions, where the magnitude of slip scales with displacement [5, 9, 17, 30–35]. This serves as a fundamental prediction we may see in our study area, making this region a good place to perform tectonic geomorphology analyses. Moreover, this gradient in tectonic activity provides an opportunity to calibrate and test a stream power model of river incision [36]. To accomplish our analyses, we use (1) channel morphology metrics including channel steepness values, knickpoint distributions, and transient channel incision depths; (2) cosmogenic erosion rates; (3) bedrock strength data; and (4) calibrated stream power incision models to simulate the evolution of transient channels during a sustained period of base level fall. Doing so will shed light on the spatial and temporal dynamics of active Quaternary normal faults within the Northern Basin and Range region, an area where slip rate data are sparse, ambiguous, and/or poorly constrained, therefore limiting seismic hazard assessments. Furthermore, this study will highlight the utility of tectonic geomorphology in constraining fault evolution in young systems with low slip rates and total throw.

2. Background

2.1. Geologic and Tectonic Setting. The Northern Basin and Range province in Southwest Montana is home to a network of semi-isolated, fluvially connected intermontane basins bounded by Quaternary normal faults [37, 38]. Our study area is along the eastern margin of Bull Mountain and the adjacent North Boulder Basin (Figures 1(a)–1(c)). The flanking highlands of these intermontane basins, such as Bull Mountain, are remnants of the Cordilleran fold-and-thrust belt [38] which were primarily formed under three tectonomagmatic events that overlap in space, namely, (1) Sevier fold and thrust belt deformation, (2) calc-alkaline magmatism, and (3) Laramide basement uplifts [37–39]. The basement-cored Laramide uplifts and Sevier fold-and-thrust belt development are the two primary tectonic components responsible for the development of the Cordilleran thrust belt that began in the late Jurassic and continued its development into the late Paleocene to early Eocene [38]. Widespread arc volcanism and emplacement of Cordilleran batholiths also occurred during the late cretaceous to early Eocene time [38, 40, 41], creating the Boulder Batholith (81-73 and 64-61 Ma) and Elkhorn Mountain volcanics (83-80 Ma) that compose Bull Mountain [38, 42–44]. Acting as the roof of the Boulder Batholith, the Elkhorn Mountain volcanics are primarily composed of ignimbrites, dacites, rhyolites, and volcaniclastic sedimentary rocks, while the Boulder Batholith is primarily composed of intrusive bodies of granodiorite and quartz monzonite [41].

Following the Sevier fold-and-thrust belt development and Laramide uplifts, regional compression was followed by extension, thought to have initiated by the gravitational collapse of the Cordilleran orogenic wedge that affected Southwest Montana around 45 Ma and created a network of semi-isolated, fluvially connected N-S trending intermontane basins [38, 45–50]. Following the Eocene extension, a period of quiescence during the Oligocene resulted in relatively little tectonic activity and a gap in deposition, which ended during the Late Neogene to Quaternary with the onset of an increase in the extension rate that has continued into the present [5]. Previous work suggests that this increase in Late Neogene to Quaternary normal faulting and seismicity

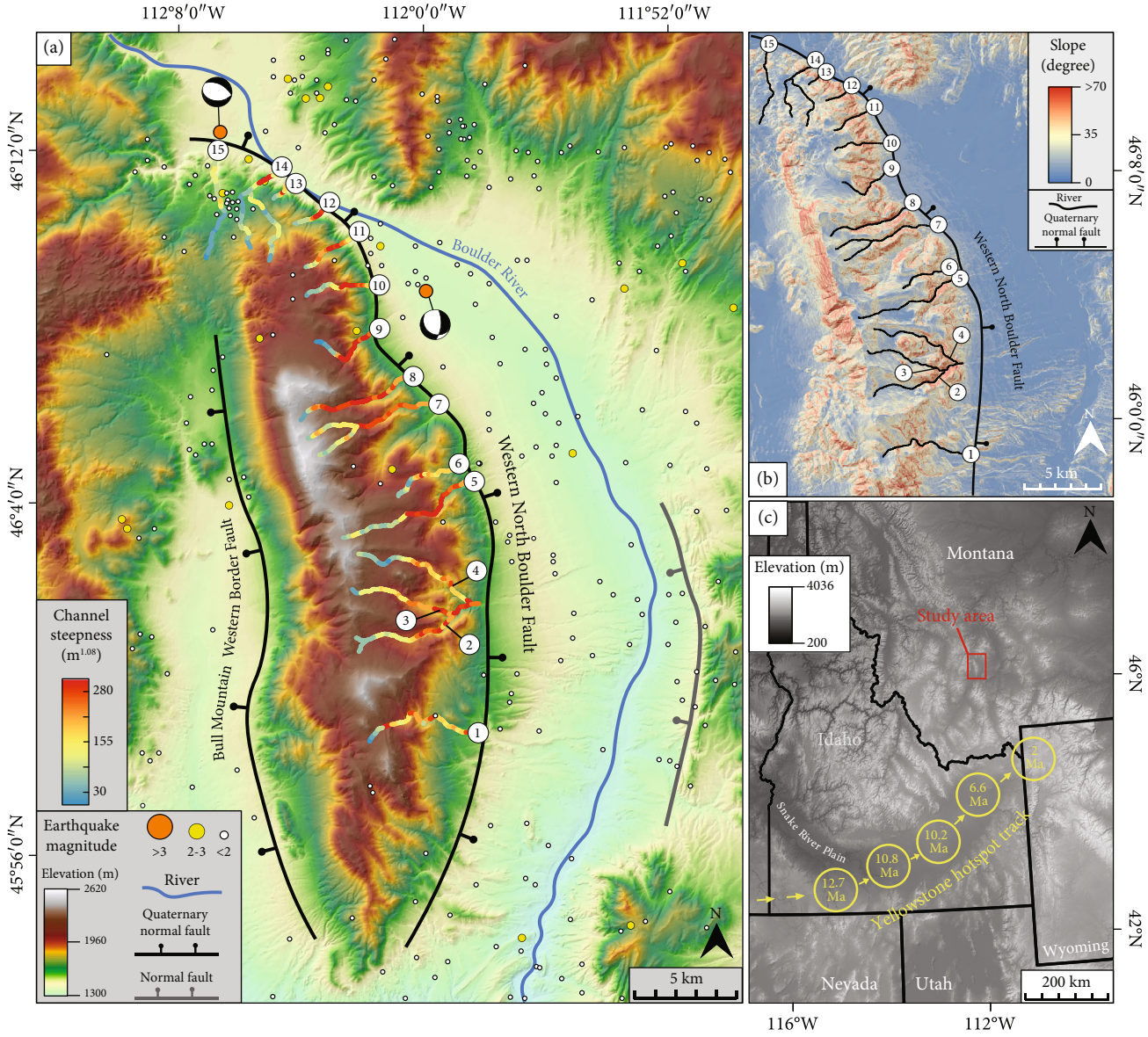

FIGURE 1: (a) Digital elevation model of the study area. The 15 bedrock channels of interest are labeled at their outlet according to their basin number and are colored by their normalized channel steepness values. The colored circles represent the magnitude of earthquakes within the region after 1980. (b) Surface slope map of the study area. Hotter colors represent higher values of surface slope. Channels that do not preserve any clear signs of transience are not shown to maintain visual clarity. (c) Elevation map of the inland northwest with the study area outlined in red. The yellow circles highlight the approximate Yellowstone hotspot track from ~12.7 to 2 Ma [54, 55].

is associated with the crustal bulge from the passage of the Yellowstone hotspot along the nearby Montana-Idaho border, beginning around 6-2 Ma and continuing into the present (Figure 1(c)) [51–55]. This ongoing phase of increased extension further reactivated and segmented the intermontane basins within the Northern Basin and Range province, creating the regional topography observed today (Figure 1(c)) [38, 40, 52].

Studies have suggested that slip along the Western North Boulder fault (Figures 1(a)–1(c)) has been ongoing at a rate of <0.2 mm/yr since at least 0.75 Ma and, as a result, induced the incision and deposition of alluvial fans that resulted in as much as 120 m of offset on the Western North Boulder Basin alluvial fan surface (Figure 1(c)) (Johns et al., 1982; U.S. Geological Survey and Montana Bureau of Mines and Geology, Quaternary fault and fold database for the United States). These fans inhibit the persistence of any fault scarps or footwalls on ≥10 m DEMs; therefore, the timing and magnitude of fault slip along the Western Boulder fault are not well constrained. Regardless, combined studies constrain the initiation of increased extension around 6 to 0.75 Ma ([51–53]; Johns et al., 1982; [54, 55]). We aim to analyze the transient channels of eastern Bull Mountain to improve constraints on the spatial and temporal slip rates across the Western North Boulder fault zone and help characterize Northern Basin and Range normal faulting histories. Furthermore, we strive to illustrate the utility of tectonic geomorphology in constraining normal fault evolution in young systems where

slip rates and total throw are too low to extract via other geologic methods.

2.2. Transient Incision of Bull Mountain. Transient landscapes in the Northern Basin and Range province in Southwest Montana provide a record of the region's extensional tectonic history [56, 57]. Fifteen channels draining along the Western North Boulder fault exhibit a striking contrast in topographic gradient, with a gentle, low relief relict landscape situated upstream at higher elevations and a steep, high relief transient landscape situated at lower elevations (Figures 1(a) and 1(b)). Because the hillslope gradients increase across this transition and show no evidence of glaciation or stream capture that could produce nontectonic pulses of incision [58, 59], we interpret these morphologies to be indicative of a headward-advancing landscape adjustment to a change in the rate of base level fall. Furthermore, the proximal Western North Boulder fault has been actively extending the North Boulder Basin since at least 0.75 Ma (Johns et al., 1982), and this tectonic activity could change the rate of base level fall for these streams. We therefore argue that the transient incision within these channels provides a record of the ongoing extension along the Western North Boulder fault. Channels that do not preserve clear evidence of transience are not shown in Figures 1(a) and 1(b) to maintain visual clarity. For example, our study area does not extend to the southern portion of the Western North Boulder fault and Bull Mountain because no transience is preserved in this area, which could be due to variations in erosional processes, drainage area, bedrock properties, or fault dynamics. Along the 15 channels where transience is ongoing, we aim to improve constraints on the spatial and temporal slip rates across the Western North Boulder fault zone by applying channel morphometrics, cosmogenic erosion rates, bedrock characteristics, and calibrated stream power incision models.

3. Methods

We performed a series of channel profile analyses to quantify local channel slopes and their respective drainage area values, spatial distribution of knickpoints, and transient channel incision depths along the 15 channels actively responding to an increase in base level fall (Figures 1(a) and 1(b)). We measured bedrock fracture density and Schmidt hammer rebound values in order to assess variations in rock strength, which can influence the transient behavior of rivers [14, 60–63]. We use a numerical stream power model to constrain the rates of pre- and postbase level fall and river incision parameters for all 15 channels in our study area. Catchment-averaged erosion rates have been calculated to provide further constraints on these values.

3.1. Channel Profile Analysis. We extract the elevation, distance, and contributing drainage area from a 10 m DEM (USGS, 2018) for each channel by delineating a Topotoolbox v2 flow direction algorithm in MATLAB that follows a path of 10 m pixels along reaches draining >2 km^2 [64, 65]. Elevation data is smoothed over a 5-pixel smoothing window (50-70 m depending on flow path) to remove inherent noise in the river profile [11, 15].

3.2. Channel Steepness Index. Channel steepness index is a measure of river slope relative to the upstream contributing drainage area that can be used to infer relative changes in base level fall across a landscape, assuming that the channels in the region were originally in dynamic equilibrium (i.e., the rate of erosion equals the rate of base level fall) prior to the change in base level fall [15, 18]. For rivers in dynamic equilibrium, local channel slope (S) can be expressed as a power-law function of the contributing drainage area (A) [15]:

$$S = \left(\frac{U}{K}\right)^{1/n} A^{-(m/n)}, \tag{1}$$

where U is the rock uplift (or base level fall), K is the bedrock erodibility, and m and n are the exponents that depend on channel geometry, basin hydrology, and incision processes [1, 66, 67], respectively, and strongly influence the transient behavior of bedrock rivers [21, 36]. This equation predicts that if erodibility and rock uplift are spatially uniform, then channel slope (S) will have a power law relationship with the drainage area (A). Indeed, this relationship leads to the concave profiles of equilibrated streams (Figure 2). The cofactor on the right-hand side of equation (1) is often referred to as channel steepness (k_s) [68, 69]:

$$k_s = \left(\frac{U}{K}\right)^{1/n}. \tag{2}$$

The drainage area (A) exponent in equation (1) is referred to as the channel concavity (θ) ([68]; Hack, 1973; [13, 69]).

$$\frac{m}{n} = \theta. \tag{3}$$

Substituting equations (2) and (3) into equation (1) yields

$$S = k_s A^{-\theta}. \tag{4}$$

To compare the slopes of channels that vary in size, we evaluate channel steepness by dividing channel slopes by the upstream drainage area with an assumed reference concavity (θ_{ref}). This normalized value is referred to as k_{sn} [15, 62]. We use a fixed reference concavity index that is the average of all 15 relict channel concavities (0.54, Table 1) which is approximate to the concavity values commonly used by other studies in the region [11] and consistent with other empirical studies for river profiles near equilibrium [10, 13, 15, 18, 70].

In landscapes responding to an increase in base level fall, low normalized channel steepness (k_{sn}) values at higher elevations are interpreted as the remainder of a relict profile equilibrated to the previous rate of rock uplift, while high k_{sn} values represent the actively incising transient profile that is adjusted to the increased rate of base level fall (Figures 1(a)

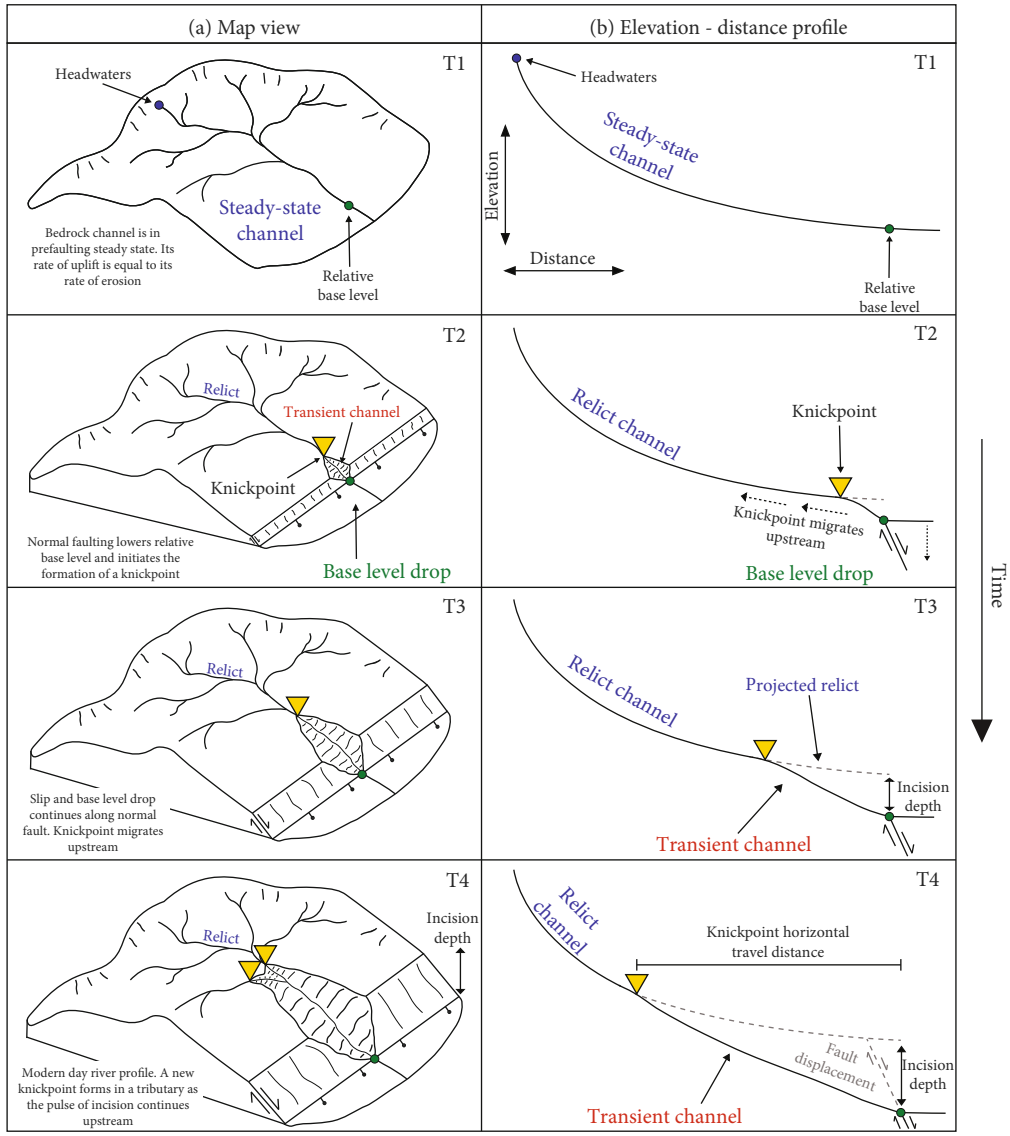

Figure 2: Evolution of a transient river bedrock profile through time. (a) Shows an aerial view of bedrock channel under a pulse of transient incision. (b) Displays the elevation-distance profile of the same bedrock river under transient incision. Time begins in the first row and then advances into the following rows.

Table 1: Channel morphology and erodibility relationships according to the stream power equation.

Relationship	$n < 1$	$n = 1$	$n > 1$
KP horizontal travel distances in the X-space scale with the timing of base level fall.	Yes	Yes	Yes. Also is dependent on $U(t)$
KP horizontal travel distances in the X-space scale with K when initiation of base level fall is the same.	Yes	Yes	Yes
KP elevation scale with K.	No	No	Yes
Normalized channel steepness values scale with the rate of base level fall.	Yes, scales to the n power	Yes, scales to the n power	Yes, scales to the n power
Normalized channel steepness values reflect the ratio of the base level fall rate to K.	Yes	Yes	Yes

and 2). The relationship between the relict and transient k_{sn} values have been shown to represent the relative change in the old and new rate of uplift, erosion, or base level fall [9, 14, 17, 18, 71–74].

3.3. X-Plots (Chi-Plots). In order to remove the effect of the drainage area and minimize inherent noise in topographic data, we also analyze channel profiles in X-space (Chi-space) following the integral method [21]. Separating variables in

equations (1)–(4), assuming U and K are spatially invariant, and integrating them from position upstream of base level (x_b) to x yields [21, 75]

$$z(x) = z(x_b) + \left(\frac{U}{KA_0{}^m}\right)^{1/n} X, \tag{5}$$

$$X = \int_{x_b}^{x} \left(\frac{A_0}{A(x)}\right)^{\frac{m}{n}} dx. \tag{6}$$

where x_b is the base level, x is the distance upstream, z is the elevation, A_0 is a reference drainage area (set to 10^6 m^2), and X is the transformed distance upstream. Channel profiles in X-space are known as "X-plots," where z is plotted against X. A steady-state channel with uniform conditions will have a linear X-plot, while a transient profile will have linear relict and adjusted reaches with slopes dependent on their respective k_{sn} values (Figures 3(a)–3(c)) [21, 75].

3.4. Knickpoints. Equation (1) predicts that a temporal change in base level fall will initiate a steepening of the channel gradient at the channel outlet and will progressively migrate upstream until the channel gradient has reached equilibrium with the new rate of base level fall (Figure 2) [1]. The steep, headward propagating reach is known as the transient channel, while the upstream portion is deemed the relict (Figures 2 and 3(a)–3(c)). The knickpoint is the transition from the low eroding relict reach that has not been impacted by the new rate of base level fall to the steep, swiftly eroding transient profile that is adjusting to the new rate of base level fall (Figures 2 and 3(a)–3(c)). Knickpoints are identified as breaks in a river's slope area relationship (Figures 3(a)–3(c)) [15]. These breaks can manifest as either a sharp discontinuity in channel slope or as the top of a convex-upward reach called a knickzone [11]. We define knickpoints as the lowest elevation of the relict reach where it diverges from a straight line in X-space (Figure 3(b)) using a MATLAB script developed by [11] containing functions from Topotoolbox v2 [64, 65].

The upstream propagation of knickpoints following a new rate of base level fall can be measured in both vertical and horizontal travel distances relative to the channel outlet (Figures 3(a) and 3(b)) [9, 11, 14]. The vertical and horizontal knickpoint migration rates have different relationships with U, n, and K, where a knickpoint's horizontal celerity is dependent on the new uplift rate (U) only when n>1 and vertical celerity are dependent on K only when n >1 [11].

3.5. Incision Depths. Transient channel incision depths reflect the total base level fall since fault initiation minus relict exhumation (Figure 2) [9–11, 76, 77] which is independent of catchment size [78]. We quantify the transient channel incision depths to provide constraints on the magnitude of base level fall along the outlet of each stream profile. We measure incision depths by projecting the relict reach downstream of the knickpoint (paleoriver) by using the relict reference concavity (0.54) and K_{sn} values in equation (4) (e.g., [77]) and taking the elevation difference from the paleo- to modern stream outlet, as shown in Figure 3(b).

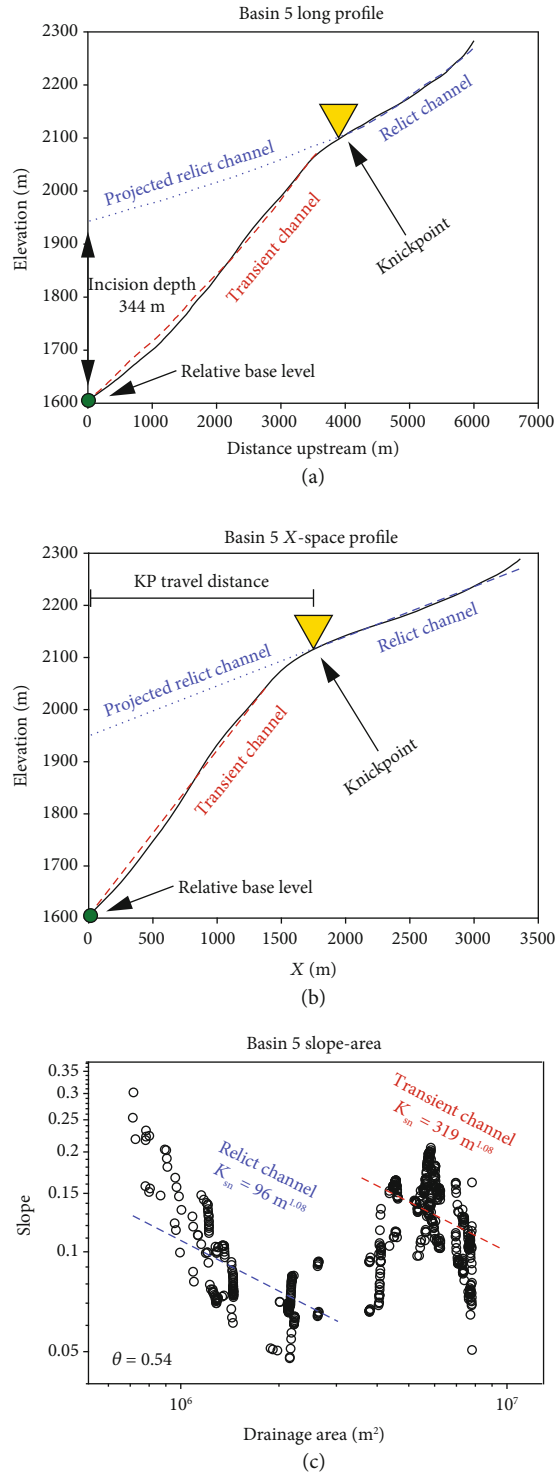

FIGURE 3: (a)–(c) Examples of river profile analysis performed on basin 5. (a) Distance-elevation profile of basin 5. (b) Basin 5 profile in X-space. (c) Slope-drainage area data for basin 5 in log space. The knickpoint is determined by the slope break in the distance-elevation profile, X-space profile, and the slope-area data..

The downstream projection of the relict profile at the fault is [11]

$$z_{\text{relict projected}} = z_{\text{KP}} - \left(\frac{U_{\text{initial}}}{K}\right)^{1/n} A_0^{-(m/n)} X_{\text{KP}},$$
$$I = z_{\text{relict projected}} - z(x_b) = t(U - U_{\text{initial}}), \quad (7)$$

where $z_{\text{relict projected}}$ is the elevation of the projected relict outlet, z_{KP} is the elevation of the knickpoint, X_{KP} is the horizontal knickpoint travel distance in X-space, U_{initial} is the relict uplift rate (or rate of base level fall), U is the new uplift rate, and I is the incision depth. We quantify the knickpoint travel distances in X-space as the distance from the stream outlet to the location of the knickpoint (Figure 3(b)).

Through these equations, steepness indices, knickpoint distributions, and incision depths can be used to infer the spatial and temporal changes in the rate of base level fall within a given region, given that variations in climate and bedrock strength are minimal in relation to the new rates of base level fall [14].

3.6. Cosmogenic Erosion Rates. The concentration of ^{10}Be in quartz rich fluvial sediment provides long-term ($10^3 - 10^6$ yrs) spatially averaged basin-wide erosion rates [18, 79–81] and is commonly used to provide constraints on the magnitude and timing of base level fall [10, 18]. ^{10}Be in quartz is produced in proportion to the residence time of quartz grains in the uppermost few meters of the Earth's surface; therefore, larger concentrations of ^{10}Be suggest longer in situ residence time and a slower erosion rate and vice-versa [18]. We calculated relict and transient channel catchment-averaged erosion rates from cosmogenic ^{10}Be in stream sediment from basins 2, 4, 5, 10, and 14, which span the length of the Western North Boulder fault. Samples were collected in the mainstem relict and transient channels that show no sign of upstream landslides or glaciation [18, 82–84], therefore ensuring that the sediment is representative of the entire watershed. Our samples were also collected in locations with variations in upstream lithology and therefore quartz concentration (e.g., the granite-dominated relict landscape contains a higher quartz concentration than the quartz-depleted downstream transient landscape of gabbro, diorite, and rhyolite), which will be discussed as a source of uncertainty in our erosion rate calculations. Quartz separation and purification were carried out according to the methods of [85]. The isolation and measurement of ^{10}Be present within the quartz were carried out at the Purdue University PRIME AMS laboratory. Basin average cosmogenic nuclide production and erosion rates were calculated through the CAIRN method [86] and were corrected for topographic shielding.

3.7. Bedrock Strength Measurements. Bedrock strength and fracture density have an important role in the pace of the transient channel response. These properties cause variations in the bedrock erodibility parameter (K) in equation (1) and therefore modulate knickpoint migration rates [14, 60–62, 87]. To account for these effects, we collected nearly 5000 Schmidt hammer rebound values and over 150 bedrock fracture density values for each of the main lithological units along the 15 transient channels (Selby 1980). Schmidt hammer measurements were taken in groups of 60 consecutive readings distributed across bedrock surfaces that show minimal signs of weathering and fracturing [60]. Fracture density measurements were taken in the same proximal locations of Schmidt hammer measurements. Fracture density values were measured by counting the number of fractures or joints that intersect a meter-long transect of bedrock. Fracture density is therefore reported here as the number of fractures per meter of exposed bedrock. At each location, we used a horizontal and vertical transect to measure fracture density.

3.8. Stream Power Model. We use a first-order upwind 1-D stream power-based river incision model to constrain the spatial and temporal patterns of fault slip along the Western North Boulder Fault. The goal of the model is to determine the rate and initiation time of base level fall required for the knickpoints to travel to their current locations. We test a wide range of uplift rates (or rates of base level fall), slope exponent (n) values, and bedrock erodibility (K) values in our simulations (Table 2). We use a weighted sum of square deviation (WSSD^2) misfit analysis to calibrate acceptable ranges of these values.

The governing equation used in the incision model is the stream power equation based on detachment limited bedrock river incision, which solves for the change in elevation (z) with time (t) [66, 69]:

$$\frac{dz}{dt} = U(t) - E = U(t) - KA^m S^n, \quad (8)$$

where E is the erosion. We test changes in rock uplift (U) with time (t) as a (1) step function (also known as a stair function, or instantaneous increase) and as a (2) linear increase (from fault initiation to the present) in base level fall at the outlet of all 15 channels. We also test the time prior to present that this increase in rock-uplift occurred (i.e., the fault initiation time) with values ranging from 0.1 to 9 Ma. This range extends beyond the known constraints within the region [38, 52, 54] ensuring we are exploring all plausible scenarios. Prior to the change in rock uplift, the rivers are initialized as a steady-state river meant to reproduce the observed relict reaches.

We define the initial relict (and lower rates) of base level fall ($U(t = 0)$) as U_{initial}. We test a range of relict base level fall (U_{initial}) rates according the relationship between bedrock erodibility, uplift, and channel steepness:

$$k_{sn} = \left(\frac{U_{\text{initial}}}{K}\right)^{1/n}. \quad (9)$$

Assuming that the relict landscape is in steady state (i.e., relict uplift rates are equal to relict erosion rates), we use the CRN-derived relict and basin-wide erosion rates from basins 4, 5, 10, and 13 to constrain a range of 3 relict uplift (U_{initial}) rates ($2 \times 10 - 5$, $5 \times 10 - 5$, $8 \times 10 - 5$ m/yr; Table 2). In each

Table 2: Summary of parameters used within each model run. Each run represents 10,000 1-dimensional river profile simulations.

Model run	Rate of base level fall	$U_{initial}$ (m/yr)	$U(t)$ (m/yr)	n	K
1	Step function	2*e*-5	2*e*-5 to 1*e*-3	0.67	1×10^{-7} to 1×10^{-4} $m^{0.28}$/yr
2	Step function	2*e*-5	2*e*-5 to 1*e*-3	1	1×10^{-8} to 1×10^{-5} $m^{-0.08}$/yr
3	Step function	2*e*-5	2*e*-5 to 1*e*-3	1.5	1×10^{-9} to 1×10^{-6} $m^{-0.62}$/yr
4	Step function	5*e*-5	5*e*-5 to 1*e*-3	0.67	1×10^{-7} to 1×10^{-4} $m^{0.28}$/yr
5	Step function	5*e*-5	5*e*-5 to 1*e*-3	1	1×10^{-8} to 1×10^{-5} $m^{-0.08}$/yr
6	Step function	5*e*-5	5*e*-5 to 1*e*-3	1.5	1×10^{-9} to 1×10^{-6} $m^{-0.62}$/yr
7	Step function	8*e*-5	8*e*-5 to 1*e*-3	0.67	1×10^{-7} to 1×10^{-4} $m^{0.28}$/yr
8	Step function	8*e*-5	8*e*-5 to 1*e*-3	1	1×10^{-8} to 1×10^{-5} $m^{-0.08}$/yr
9	Step function	8*e*-5	8*e*-5 to 1*e*-3	1.5	1×10^{-9} to 1×10^{-6} $m^{-0.62}$/yr
10	Linear increase	2*e*-5	2*e*-5 to 1*e*-3	0.67	1×10^{-7} to 1×10^{-4} $m^{0.28}$/yr
11	Linear increase	2*e*-5	2*e*-5 to 1*e*-3	1	1×10^{-8} to 1×10^{-5} $m^{-0.08}$/yr
12	Linear increase	2*e*-5	2*e*-5 to 1*e*-3	1.5	1×10^{-9} to 1×10^{-6} $m^{-0.62}$/yr
13	Linear increase	5*e*-5	5*e*-5 to 1*e*-3	0.67	1×10^{-7} to 1×10^{-4} $m^{0.28}$/yr
14	Linear increase	5*e*-5	5*e*-5 to 1*e*-3	1	1×10^{-8} to 1×10^{-5} $m^{-0.08}$/yr
15	Linear increase	5*e*-5	5*e*-5 to 1*e*-3	1.5	1×10^{-9} to 1×10^{-6} $m^{-0.62}$/yr
16	Linear increase	8*e*-5	8*e*-5 to 1*e*-3	0.67	1×10^{-7} to 1×10^{-4} $m^{0.28}$/yr
17	Linear increase	8*e*-5	8*e*-5 to 1*e*-3	1	1×10^{-8} to 1×10^{-5} $m^{-0.08}$/yr
18	Linear increase	8*e*-5	8*e*-5 to 1*e*-3	1.5	1×10^{-9} to 1×10^{-6} $m^{-0.62}$/yr

model run, the relict reference concavity (0.54), $U_{initial}$, K, and n values are applied to reach a steady-state profile (i.e., paleoriver profile) within all 15 channels. Starting at the equilibrium state, the downstream end node of the paleoriver profile is lowered to its modern position through time (Figures 4(a)–4(c)). We test a wide range of postacceleration uplift rates ($U(t)$) that range from $U_{initial}$ to $1 \times 10 - 3$ m/yr, which encapsulates the estimated rates of base level fall for the Western North Boulder fault (>0.2 mm/yr, Johns et al., 1982) and other studies in the Northern Basin and Range province [33, 82]. For consistency, we focus on the results from the mean $U_{initial}$ ($5 \times 10 - 5$ m/yr) simulations. We report the results with the minimum and maximum $U_{initial}$ simulations in the supplementary materials (available here).

The exponent for channel slope (n) in equations (8) and (9) strongly influences transient channel behavior [1, 11] and is postulated to reflect dominant incision processes, with plucking consistent with n values of ~0.67 to 1 and abrasion consistent with n values of ~1.5 [67]. Because these incision processes are controlled by bedrock properties like tensile strength [3], compressive strength [60], and fracture density [61, 88], it is important that we recognize potential variations in n in our lithologically diverse study area. Therefore, we test all simulations with n values of 0.67, 1, and 1.5.

We test a wide range of bedrock erodibility (K) values ($1 \times 10 - 7$ to $1 \times 10 - 4$ $m^{0.28}$/yr for $n = 0.67$; $1 \times 10 - 8$ to $1 \times 10 - 5$ $m^{-0.08}$/yr for $n = 1$; $1 \times 10 - 9$ to $1 \times 10 - 6$ $m^{-0.62}$/yr for $n = 1.5$) that capture the range of calibrated stream power erodibility values found in other studies (i.e., [10, 19, 62, 89–91]). We assume that erodibility is constant along an individual river profile, which is reasonable for uniform lithology [10, 13]; yet, the lithological differences among different drainage basins in the study area (Figure 1(b)) will be expected to produce a larger amount of variability within the model results. A summary of the parameters used within each model run is displayed in Table 2. Each model run contains a specific n and $U_{initial}$ value and 100 intervals of base level fall (U) and bedrock erodibility (K) values, resulting in 10,000 profile simulations.

We further constrain the range of bedrock erodibility (K) values by combining equations (1), (3), and (8) to form a relationship between the erosion rate and channel steepness [10]:

$$E = Kk_{sn}^{n}. \tag{10}$$

We use the CRN-derived erosion rates for E and the mean relict and transient channel steepness (k_{sn}) values in equation (10) to solve for K. We compare these K values to those constrained in the incision simulations to further assess the confidence in our results.

3.9. Model Fit Assessment. We apply a goodness of fit weighted sum of square deviations ($WSSD^2$) analysis scheme to evaluate the ability for each model run to reproduce the modern profile [29, 92]:

$$\mathrm{WSSD}^2 = \frac{1}{N - \nu - 1} \sum_{i}^{N} \left(\frac{\mathrm{sim}_i - \mathrm{obs}_i}{\mathrm{tolerance}} \right)^2, \tag{11}$$

where N is the number of nodes along the profile, ν is the number of free variables, sim_i is the simulated elevation at node i, and obs_i is the smoothed observed modern profile at node i. The vertical accuracy of the 10 m USGS DEM is reported to be ±1.87 m [93]. To account for the inherent

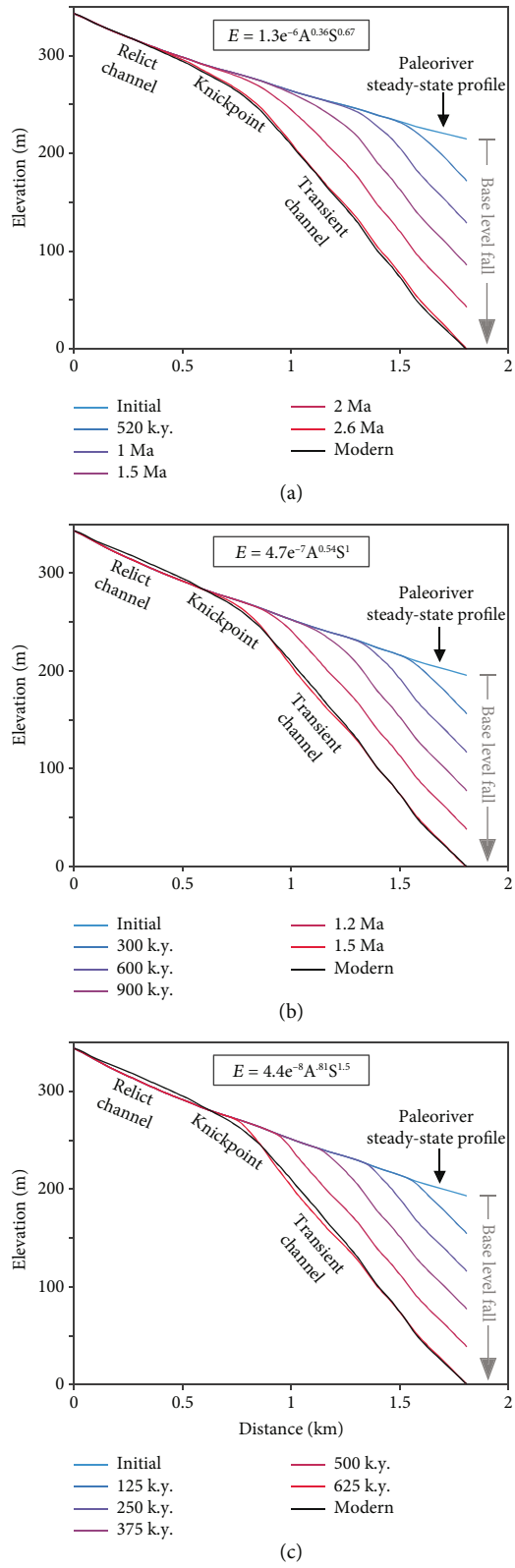

FIGURE 4: (a)–(c) Example best fit river profile simulations for basin 10 during a step function in base level fall. (a) Displays a base level fall simulation with a rock erodibility (K) value of 1.3e-6 and a slope exponent (n) value of 0.67, (b) rock erodibility (K) value of 4.7e-7 and a slope exponent (n) value of 1, (c) rock erodibility (K) value of 4.4e-8, and a slope exponent (n) value of 1.5. The colored lines represent the evolution of the profile through time. The initial paleoprofile was reconstructed using the relict k_{sn} value back calculated from the bedrock erodibility value according to equation (5). A represents drainage area, while S represents channel slope. All simulations are acceptable fits with a weighted sum of square deviations ($WSSD^2$) value less than 1.

Table 3: Basin characteristics.

Basin	Distance north along strike (km)	Drainage area (km^2)	Relict drainage area (km^2)	KP horizontal travel distance in X-space (m)	KP elevation (m)	Incision depth (m)	Relict K_{sn} ($m^{1.08}$)	Transient K_{sn} ($m^{1.08}$)	Relict concavity (θ)
1	0	7.43	4.01	2056	1923	124	131	216	0.52
2	3.4	15.8	5.29	1237	1953	183	122	285	0.78
3	5.8	5.72	1.11	2062	2097	237	116	276	0.55
4	7.4	6.39	1.97	2122	2073	264	88	223	0.67
5	9.0	7.71	2.16	1864	2128	344	96	319	0.68
6	11	2.89	0.87	1919	1985	207	90	210	0.53
7	14.4	5.11	1.73	2048	2103	236	150	292	0.38
8	16.4	5.62	0.48	2371	2358	497	59	306	0.35
9	19	4.49	0.8	2099	1970	355	212	383	0.74
10	22.2	2.18	1.59	893	1937	203	93	382	0.58
11	23.4	1.95	0.13	1626	1936	246	94	269	0.44
12	25.6	0.61	0.2	959	1726	59	158	228	0.21
13	27	0.82	0.17	957	1648	110	70	241	0.28
14	28.5	6.4	5.93	451	1615	117	123	539	0.43
15	29.8	13.05	3.0	1175	1638	99	35	128	0.89

vertical noise, we define the tolerance to be 10 m, which is nearly 5 times the vertical accuracy. $WSSD^2$ values above 1 suggest a poor fit well beyond the noise of the modern DEM, while $WSSD^2$ values below 1 suggest a close reproduction of the modern profiles. A $WSSD^2$ value of 2 means that the average difference between the observed and simulated profiles is ~14 m. Simulations that result with a $WSSD^2 \leq 1$ are considered acceptable fits.

3.10. Stream Power Metrics. Several relationships between the measured channel metrics and simulation results should exist (i.e., observed knickpoint horizontal travel distances in X-space scale with the modeled timing of base level fall) if the 15 transient channels in the study area behave in a manner consistent with the stream power model of a step function in base level fall (Table 1) [11, 17, 94]. For these relationships, we assume spatially and temporally constant K, n, and m. It is important to note that horizontal and vertical knickpoint migration rates have different relationships with U, n, and K (Table 2) [11]. We report the relationships in Table 2 to assess if the behavior of the 15 channels in our study area is consistent with the stream power equation.

4. Results

4.1. Channel Morphology and Knickpoint Distributions. The pattern of normalized channel steepness (k_{sn}) mimics the distribution of hillslope gradients proximal to channels, where low channel steepness values are found in the flat, upstream relict landscape, while high channel slopes are found in the steep, narrow transient reaches of each channel (Figures 1(a) and 1(b)). Steepness increases by an average factor of 2.9 from relict ($109 \pm 44\ m^{1.08}$ average) to transient ($286 \pm 96\ m^{1.08}$ average) reaches (Table 3), which should roughly reflect the difference between the relict ($U_{initial}$) and new (U) rates of base level fall depending on the slope exponent (n) value [15]. Most relict and transient channel segments appear to be linear on X plots (Figure 5(d)), confirming that the reference concavity (θ) of 0.54 is a reasonable estimate of the concavity of the relict and transient channels along Bull Mountain [17, 21, 75].

All 15 transient channels contain a single knickpoint with a slope-break morphology (Figures 5(a)–5(d)). We observe that the knickpoints within most of the profiles contain a more stretched, elongated knickzone that is consistent with n values<1, rather than a sharp slope break knickpoint zone that is found with n values ≥1 (Figure 5(d)) [11, 21, 36].

Knickpoint elevations and transient channel incision depths have a general pattern consistent with normal fault displacement—higher values towards the center of the Western North Boulder fault (Figures 5(a)–5(c)). Incision depth in basin 1 at the southern end is ~124 m, which increases to 497 m incision in basin 8 and then decreases to 99 m incision by basin 15 (Figures 5(a) and 5(b), Table 3). There is some variability from the general trend, including relatively high (basin 8, 497 m) and low (basin 6, 207 m; basin 7, 236 m; and basin 12, 59 m) incision depths (Figure 5(b)). These variations in knickpoint elevation could be attributed to localized variations in the temporal and spatial patterns of base level fall (i.e., due to normal fault linkage) [17], noise within the DEM [15], or deviations in relict steepness values that lead to inaccurate paleoriver reconstructions. Nonetheless, this elliptical pattern of transient channel incision depths suggests that the duration (i.e., initiation timing) and/or magnitude of base level fall is the highest near the center of the fault around basin 8 and minimizes towards the north end near basin 14, which is consistent with the general model of the slip distribution along a normal fault [17, 33].

The knickpoint travel distances in X-space are similar (~2 km) from basins 1 to 9 and then decrease northward

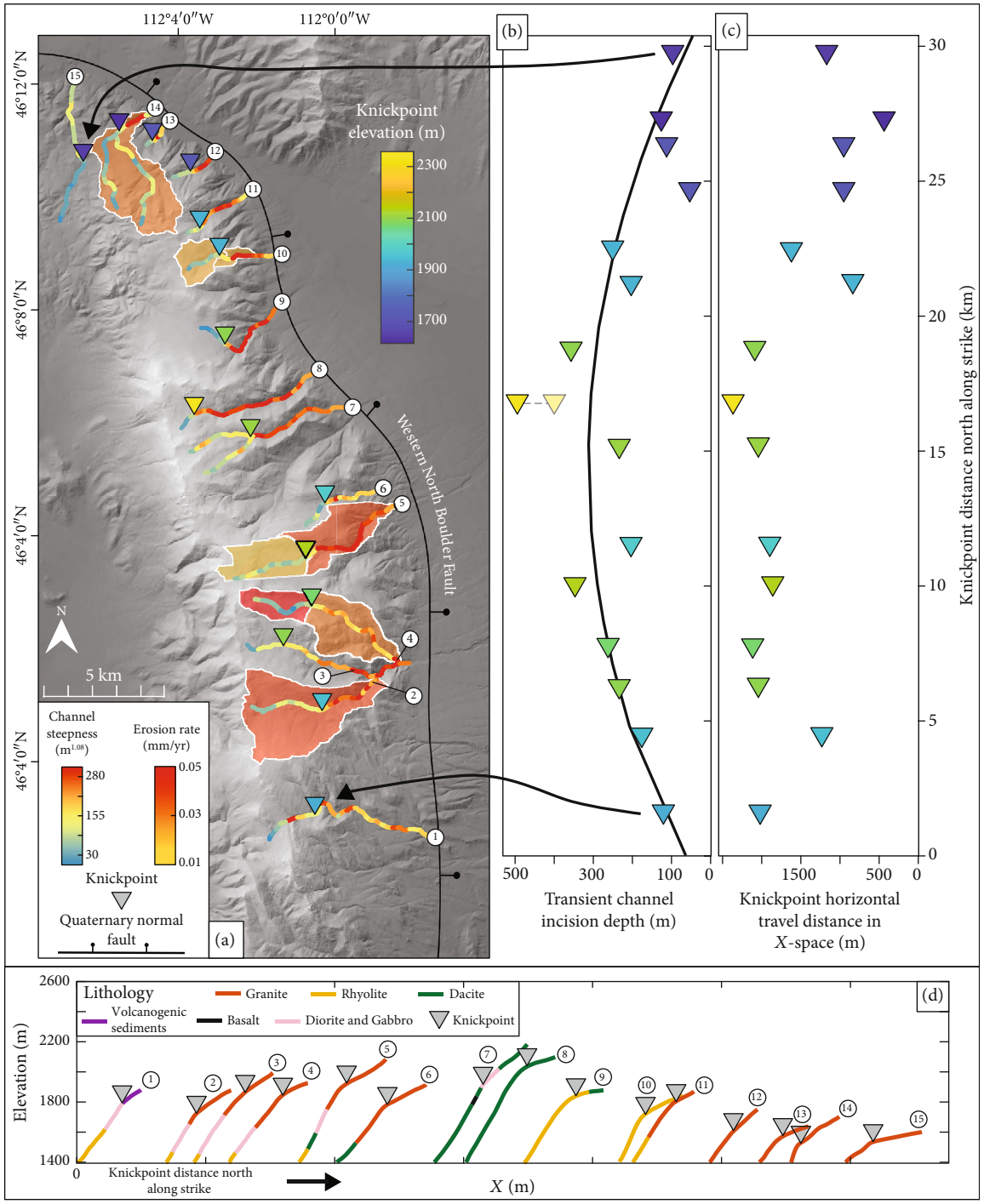

Figure 5: (a)–(d) Channel profile analysis results. (5) Digital elevation map of the study area with bedrock channels colored by their normalized steepness values. The triangles represent the locations of the knickpoints for each channel, colored by their elevation above sea level. The white lines denote the transient and relict basins where cosmogenic nuclide data was collected, colored by the calculated erosion rates at the outlet of each basin. (b, c) show the transient channel incision depths and knickpoint horizontal travel distance values in X-space, ordered distance north along strike of the Western North Boulder fault. (d) X-profiles for all 15 channels, colored by their respective lithologies. Profiles are ordered by their knickpoint distance north along strike of the fault.

along strike from basins 9 to 15 to ~1 km (Figure 5(c)). There is some variability from this general trend, including relatively low (basin 2, 1237 m; basin 10, 893 m) and high (basin 15, 1175 m) horizontal travel distances in X-space (Figure 5(c)). These variations could be explained through local variations in the timing of base level fall initiation, channel narrowing effects [9, 14, 23, 95–98] or variations in the erosional resistance of bedrock [60, 62]. Because the horizontal travel distance of knickpoints formed at the same time should scale with the drainage area [28, 71, 99, 100] and

therefore plot at the same X values [11, 17, 21, 94], these data suggests that the initiation of base level fall is similar in the south to middle portion of the fault and then relatively later in the northern end of the fault.

4.2. Cosmogenic Erosion Rates. Beryllium concentrations are consistent with the expectation of the general pattern of hillslope and river steepness. Concentrations in the relict landscape of basins 4, 5, and 10 range from ~28 to 78×10^4 atoms/g SiO_2, resulting in erosion rates of 0.019 ± 0.001 to 0.049 ± 0.002 mm/yr (Table 4, Figure 5(a)). Concentrations taken at the mouth of basins 2, 4, 5, 10, and 14, which include both relict and transient topography (basin-wide), range from ~34 to 61×10^4 atoms/g SiO_2, resulting in erosion rates of 0.022 ± 0.002 to 0.042 ± 0.001 mm/yr (Table 4, Figure 5(a)). Using a drainage area weighted mixing model [101] along with rates of 0.019 ± 0.001 to 0.049 ± 0.002 mm/yr for the relict, we back out an estimated range of 0.021 ± 0.002 to 0.04 ± 0.001 mm/yr for the transient/adjusted portion of the landscape in basins 4, 5, and 10 (Table 4, Figure 5(a)).

Overall, no observable erosion rate trends exist from the northern to southern relict or adjusted basins. Relict, adjusted, and basin-wide erosion rates do not show a significant pattern of increasing with channel steepness (Figure 5(a)), and we observe no relationship between the erosion rate and lithology. For example, in basin 4, the relict erosion rate (0.049 ± 0.002 mm/yr) is higher than the transient/adjusted (0.031 ± 0.001 mm/yr), deviating from the expectation of the increasing erosion rate within increasing channel steepness. We discuss these discrepancies below.

4.3. Bedrock Strength Measurements. The Schmidt hammer values show little variation northward along strike, with median values having a narrow range from 57 to 65 (Figures 6(a) and 7). This suggests that all major lithological units have similar compressive strength ([60, 62]; Selby, 1980). Although incision into bedrock streams occur through breakage in tension, not compression, studies have shown that the compressive strength of rock is strongly correlated to the tensile strength of bedrock [60]. Therefore, we assume that the basin-wide tensile strength values also show no considerable variation northward along strike.

The basin-wide fracture density values, however, display considerable variation, with median values ranging from ~0.8 to 22 fractures every meter (Figures 6(b) and 7. We observe far fewer fractures in the Boulder Batholith granite and similar intrusive units than in the extrusive ignimbrites and dacite porphyries (Figure 7).

4.4. Stream Power Incision Model. The stream power model does a reasonable job reproducing all transient channel profiles in our study area (e.g., basin 10 in Figure 4) given the constraints from the erosion rate and channel morphology data. The weighted sum of square deviation ($WSSD^2$) misfit analysis results show that the percentage of acceptable fits for the simulations using a step function in the base level fall rate is significantly higher than the simulations with a linearly increasing rate of base level fall (Figure 8). This result might be expected given that the steepness of adjusted reaches in all 15 basins is near constant (Figure 5(d)) and therefore reflects more of a step function rate of base level fall [17], rather than temporally increasing. Therefore, we focus on the step function in base level fall simulations for the rest of the analysis but report the linear increase results in the supplemental.

In the step function in base level fall simulations, the fault slip initiation times vary depending on the relict base level fall (U_{initial}) rate. The simulations with the mean U_{initial} rate (5×10^{-5} m/yr) resulted in a maximum initiation time of ~6 Ma for $n = 1$ (Figure 9). Using the minimum U_{initial} rate (2×10^{-5} m/yr), the model simulations predict the oldest initiation time (max of ~8.5 Ma for $n = 1$), while simulations with the max U_{initial} rate (8×10^{-5} m/yr) produced the youngest initiation time (max of ~4.5 Ma for $n = 1$) (Supplemental Figures S5 and S6). This suggests that the lower the U_{initial} rate, the earlier the estimated initiation of new base level fall. For consistency, we focus on the step function in base level fall simulations with the mean U_{initial} rate ($5 \times 10 - 5$ m/yr) for the rest of the analysis.

Figure 9 illustrates the range of acceptable model fits for each basin and each value of n. For the simulations using a step function in base level fall, $WSSD^2$ results show that the simulations with n values of 0.67, 1, and 1.5 generated similar relative patterns for the timing of the increase in along-strike base level fall initiations (Figure 9). The magnitude of the base level fall for each of the 3 n value simulations, however, differs significantly, where the smaller the n value results in earlier initiation of base level fall (Figure 9). This makes sense as the erosion rate, which controls the rate of river response to the new base level fall, is less sensitive to changes in slope with smaller values of n [11].

All three simulations have a general along-strike trend of older initiations of base level fall in the southern to middle basins (1 to 8) along the Western North Boulder fault (median initiations from 8.8 Ma to 4.5 Ma for $n = 0.67$; 6.2 to 2.5 Ma for $n = 1$; 3.9 to 1.4 Ma for $n = 1.5$). The results in the northern basins (9, 10, 13 to 15) suggest more recent fault initiation (median initiations from 2.6 Ma to 0.5 Ma for $n = 0.67$; 1.5 Ma to 0.4 Ma for $n = 1$; 0.7 Ma to 0.2 Ma for $n = 1.5$). Basins 11 and 12 deviate from this trend with older fault initiation times similar to the southern/middle basins (median initiations from 4.6 to 4.2 Ma for $n = 0.67$; ~2.5 Ma for $n = 1$; 1.7 Ma to 1.5 Ma for $n = 1.5$). The simulations with $n = 1$ generated the highest percent of acceptable fits for all basins aside from 14 and 15, with the highest percent of fits being near 30% and the lowest percent of fits around 0.3% (Figure 9). However, even though the specified n value changes the geometry of the knickzone and transient profile (e.g., [11]), these geometric changes were not large enough to produce significant variations in the percent of acceptable fits, given the resolution of the DEM (Figures 4(a)–4(c) and 9).

4.5. Stream Power Metrics. We assess several morphologic stream power relationships between the measured channel metrics and simulation results (Table 2) to see if the 15 transient channels behave in a manner consistent with the stream

Table 4: Cosmogenic erosion rate data. Samples with basin-wide catchment areas were collected at the outlet of each basin and include both relict and transient topography. We use the default LSD Topotools CARIN method scaling scheme for calculating production rates [86, 115]. Transient/adjusted erosion rates were calculated using a drainage-area weighted mixing model.

Basin	Catchment area	Location (°N/°W)	Elevation (m above sea level)	Spallation production rate (atoms/g/yr)	Shielding factor	Quartz (g)	Be carrier (mg)	$^{10}Be/^{9}Be$ ($\times 10^{-15}$)	^{10}Be concentration (10^4 atoms/g SiO_2)	Standardization method	Basin-wide E (mm/yr)	Relict E (mm/yr)	Transient/adjusted E (mm/yr)
2	Basin-wide	46.0261/111.9790	1747	22.49	0.98823219	37.402	0.2609	737.53 ± 25.13	34.34 ± 1.17	KNSTD	0.001 ± 0.001		
4	Relict	46.0309/111.9696	2083	21.22	0.98174279	11.020	0.2581	177.75 ± 7.83	27.67 ± 1.22	KNSTD		0.049 ± 0.002	
4	Basin-wide	46.04703/112.0068	1648	25.3	0.99274165	20.259	0.2612	499.25 ± 18.54	42.94 ± 1.60	KNSTD	0.037 ± 0.001		0.031 ± 0.001
5	Relict	46.06370/112.0053	2053	24.39	0.99691589	23.981	0.2593	1078.46 ± 29.16	77.87 ± 2.11	KNSTD		0.019 ± 0.001	
5	Basin-wide	46.0766/111.9700	1606	22.18	0.98813333	34.334	0.2599	994.62 ± 24.63	50.27 ± 1.25	KNSTD	0.028 ± 0.001		0.04 ± 0.001
10	Relict	46.1492/112.0452	1950	21.76	0.99405976	29.928	0.2577	1087.25 ± 20.03	62.51 ± 11.53	KNSTD		0.022 ± 0.002	
10	Basin-wide	46.1500/112.0321	1683	21.09	0.98718503	36.171	0.2544	1304.85 ± 29.74	61.29 ± 13.51	KNSTD	0.022 ± 0.002		0.021 ± 0.002
14	Basin-wide	46.1911/112.0814	1489	18.2	0.99105326	38.169	0.2687	788.68 ± 15.62	37.06 ± 7.36	KNSTD	0.031 ± 0.001		

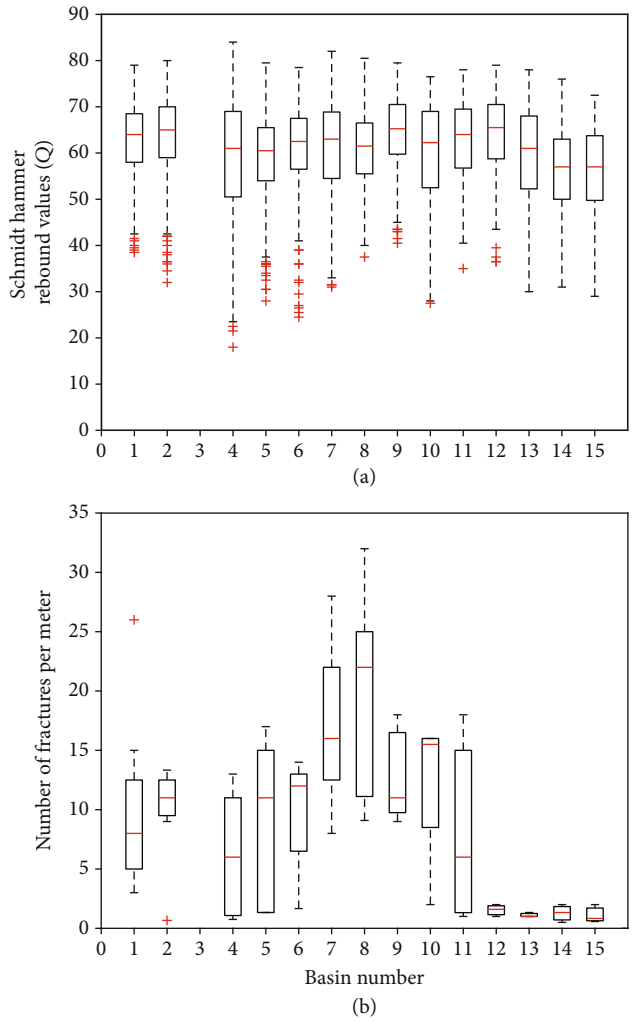

Figure 6: (a) Boxplots of the Selby mass bedrock strength (RMS) values collected along each of the 15 basins. (b) Boxplots of the bedrock fracture density values along each of the 15 basins. The red lines represent the median values, the boxes represent the 25th and 75th percentiles, the dashed lines represent nonoutliers, and the red crosses represent outliers.

power model of a step function in base level fall (Figures 10(a)–10(c)). Knickpoint horizontal travel distances in X-space have a weak pattern ($R^2 = 0.34$) of increasing with the median simulated initiation of base level fall (Figure 10(c)). Basins 7 (2 km travel distance), 8 (2.4 km travel distance), and 9 (2.1 km travel distance) have the largest deviation from the general trend and contain some of the highest travel distances in the study area.

The average knickpoint horizontal migration rates in X-space have no significant correlation ($R^2 = 0.04$) with their respective basin-wide median bedrock fracture density values (Figure 10(b)). The fracture density values also do not have any significant relationship with the median modeled bedrock erodibility values (Figure 10(b)). The mean transient channel normalized steepness (k_{sn}) values have a weak pattern ($R^2 = 0.32$) of increasing with the median modeled uplift rates (or rates of base level fall) (Figure 10(c)). Again, basins 7, 8, and 9 have the largest deviation from the general trend and contain some of the highest estimated median uplift rates (3.8×10^{-4} m/yr, 2.5×10^{-4} m/yr, and 2×10^{-4} m/yr, respectively) and fracture densities in the study area (Figures 6(c), 7, and 10(b). The fact that these three basins have the highest fracture densities in the region suggests that complex incisional processes could be occurring along their channels (i.e. ,spatially variant K and n values) causing them to deviate from stream power relationships assuming spatially uniform K, n, and m. Other factors such as drainage divide instability (potentially suggested by the differences in shape and size of these three basins as well as surrounding basins) could also explain the source of these outliers [102].

The constrained bedrock erodibility (K) values for all 15 basins range from $\sim 6.8 \times 10 - 7$ to $5.6 \times 10 - 6\,\mathrm{m}^{0.28}$/yr for the incision simulations with an n value of 0.67, $\sim 2.2 \times 10 - 7$ to $2.4 \times 10 - 6\,\mathrm{m}^{-0.08}$/yr with an n value of 1, and $\sim 1.1 \times 10 - 8$ to $3.2 \times 10 - 7\,\mathrm{m}^{-0.62}$/yr with an n value of 1.5 (Figure 11). These K values, particularly those from the $n = 1$ simulations, do not show any significant spatial trends (Figure 10(a)–10(c)). These ranges of constrained K values are consistent with the K values calculated from the CRN-derived erosion rates in equation (10) and calibrated stream power K values reported in other studies (Figure 11) [10, 19, 62, 63, 67, 89–91, 103, 104]. The observed overlap between the two methods of constraining K (i.e., from incision simulations and CRN-derived erosion rates) as well as other published studies increases our confidence in these results.

5. Discussion

Rivers are powerful tools for understanding the spatial and temporal patterns of normal fault evolution, especially where geologic and geodetic data is limited. Our results are consistent with the widely observed patterns of normal fault slip distribution/evolution (i.e., higher slip displacement along the central portion of the fault relative to the distal portions). Furthermore, our cosmogenic erosion rates and base level fall simulations provide the first quantitative spatiotemporal constraints of fault slip initiation and evolution along the Western North Boulder fault, possibly the farthest North Basin in the northern Basin and Range province that such constraints exist.

Overall, our analysis of a wide range of models using a step function in base level fall suggests that fault slip accelerated along the central portion of the Western North Boulder fault sometime between ~8.8 and 3.9 Ma. The slip initiated near basin 7 and propagated to the north and south, followed by the initiation of slip towards the south near basins 1-8 between ~6.5 and 1.4 Ma and further slip initiation near basins 9-15 in the northern end of Bull Mountain between ~2.6 and 0.2 Ma (Figure 9). The timing of base level fall strongly depends on each channel's slope exponent (n) (Figure 9), as variations in n cause the wide range of slip initiation values we report here.

Here, we discuss which range of fault initiation values are we most confident with. Combined studies have suggested that the ongoing period of increased extension within the

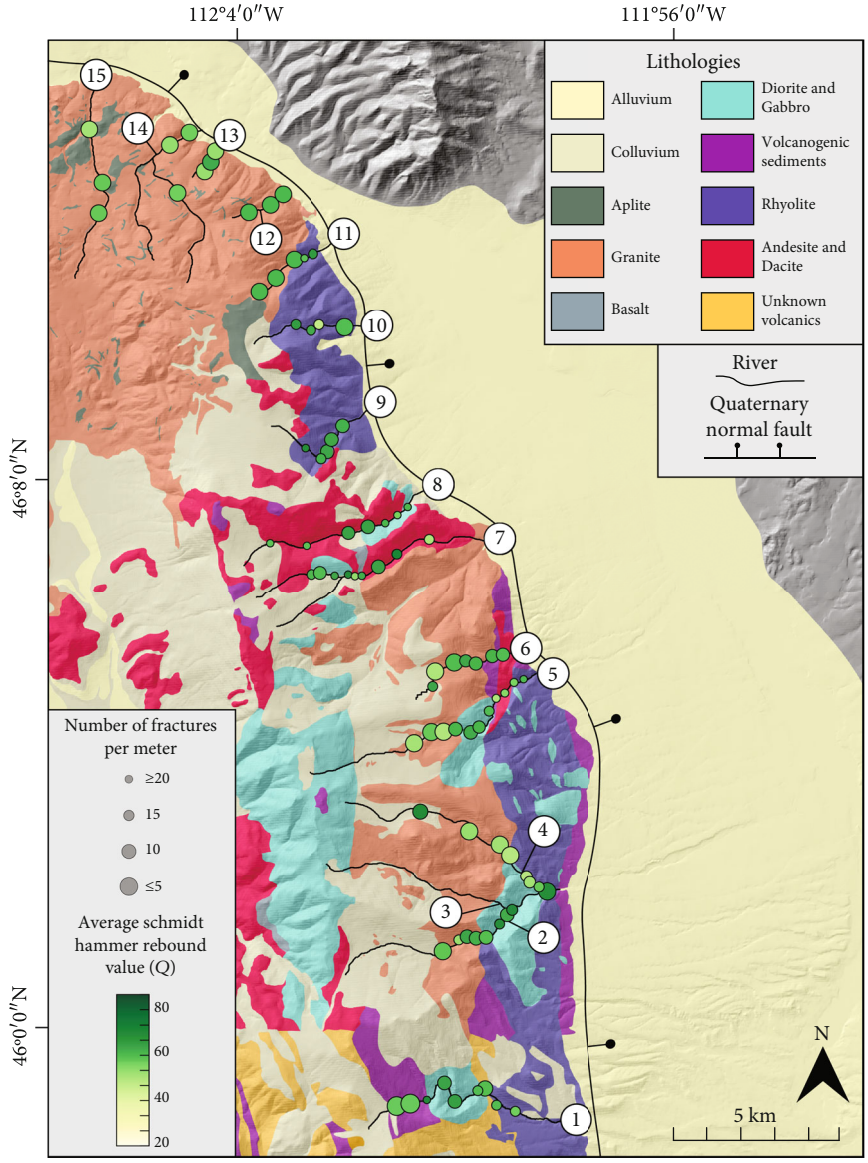

FIGURE 7: Geological map of the study area with locations of bedrock Schmidt hammer and fracture density measurements. The circle size represents the bedrock fracture density at that location, where larger circles represent a smaller number of fractures within the bedrock. The circle color represents the bedrock Schmidt hammer rebound value, where darker colors represent higher rebound values.

Northern Basin and Range province and along the Western North Boulder fault initiated sometime around 6 to 0.75 Ma and is continuing into the present ([51–53]; Johns et al., 1982; [54, 55]). The modeled timing of slip initiation for the $n = 1$ and $n = 1.5$ simulations are from ~6.2 to 2.5 and ~3.9 to 1.4 Ma, respectively, which all fit within our existing constraints. However, the $n = 1$ simulations produced a significantly higher number of acceptable fits than the $n = 1.5$ simulations. This makes sense given that the $n = 1.5$ simulations produced sharp slope break knickpoints (rather than more broad, stretched knickzones seen with the $n = 0.67$ and $n = 1$ simulations) that are not represented in any of the channels. Therefore, we place the most confidence in the $n = 1$ simulations with fault initiation times of ~6.2 to 2.5 Ma. This time range coincides well with the migrations of Yellowstone hotspot over the Idaho-Montana border from ~6-2 Ma [51–55]. Therefore, we attribute the increased extension along the Western North Boulder fault to the crustal bulge from the migrating hotspot.

5.1. Spatial-Temporal Evolution of the Western North Boulder Fault. We built an interpretive reconstruction of the Western North Boulder fault evolution using (1) incision depth values, (2) normal fault length-displacement scaling relationships, and (3) median values of base level fall rate and initiation from the step function in base level fall simulations with $n = 1$. Previous work suggests that large normal fault zones like the Western North Boulder fault can form by the nucleation and propagation of isolated fault segments, followed by an intermediate stage of overlap and linkage of these segments (i.e., soft-linked faults) that eventually evolve into larger hard-linked faults that kinematically behave like

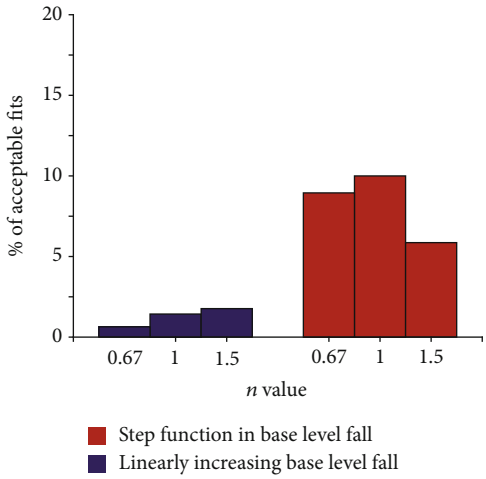

Figure 8: Comparison of percent of acceptable model fits between the step function and linearly increasing base level fall models, including model runs with three different slope exponent (n) values. The percent of acceptable fits is representative of total simulations.

isolated faults [5, 31, 35]. We adhere to these 3 stages of normal fault evolution in our interpretive reconstruction, starting with individual fault segments nucleating at the outlet of basins followed by the propagation and linkage of these segments into a large hard linked fault (i.e., the Western North Boulder fault).

When averaged over 8 orders of magnitude of normal fault data, the relationship between maximum fault displacement (D_{max}) and fault length (L) is measured to be [35]

$$D_{max} \sim \alpha L, \tag{12}$$

where $\alpha = 0.03$. We reconstruct the displacement and length of each individual fault segment from nucleation to the present by conducting a series of steps. First, we take each channel's incision depth values through the duration of base level fall and calculate the maximum fault displacement (D_{max}) through time by assuming a normal fault dip of 60°. We then calculate the length of the fault segments through time according to equation (12). Lastly, we fit the calculated fault segment displacement-length values into contours by hand through time (Figure 12). These displacement-length contours have an elliptical geometry that mirrors the widely observed pattern of the normal fault slip distribution.

Studies suggest that a rapid increase in fault slip rate occurs following the linkage of two isolated faults such that it reestablishes the displacement-length ratio ([9, 16, 17, 30, 32, 33, 105, 106], 2016; [35, 78]). This action of relatively rapid slip in zones of fault linkage is applied in our interpretive reconstruction (Figure 12).

While the two end members of fault evolution (isolated and hard-linked faults) maintain similar displacement-length ratios for the entire fault system [32, 35, 106], studies show that the dynamics of fault linkage and displacement readjustment can develop a wide range of displacement-length ratios (D max ~ 0.001-0.1 L) [30, 107–110]. We fit displacement-length contours by hand, assuming the ratio of D max ~ 0.03 L throughout the beginning (i.e., isolated faults) stages of fault evolution; yet, during the intermediate (i.e., fault linkage) and final (i.e., hard-linked faults) stages, we find it difficult to maintain this scaling and therefore relax the ratio to a range of D max ~ 0.01-0.03 L in order to maintain fault scaling relationships. Throughout all phases of fault evolution, and particularly in the zones of fault linkage, we fit the displacement-length contours to best match the constrained present distribution of total fault displacement values (i.e., black circles in Figure 12) while obeying the predicted range of scaling ratios. An illustrative guide on how we created our interpretive reconstruction is shown in the supplemental (Figure S8).

The largest incision depth is 497 m in basin 8 (Figure 5(b)), which is at least 140 m larger than its neighboring basins 7 (236 m) and 9 (355 m). The relict channel reconstruction for basin 8 has significant uncertainty due to its relatively small relict channel. Based on fault scaling relationships, we expect that the incision depth of basin 8 is overestimated. In order to obey the displacement-length ratio (equation (12)), we thus lower the incision depth of basin 8 to 400 m (462 m fault displacement), which still serves as the zone of maximum displacement and provides a more consistent displacement relationship pattern with neighboring basins (Figure 12).

Our interpretive fault evolution reconstruction begins with the nucleation of isolated fault segments that increase in displacement, propagate at the fault tips, and link together through time, developing relay ramps in the zones of linkage that accumulate extra displacement in order to maintain the range of displacement-length ratios in the resulting hard-linked faults (D max ~ 0.01-0.03 L) (Figure 12). Studies suggest that two sets of knickpoints in each channel would be expected if fault initiation was being recorded, in addition to a later linkage event [9, 78]. We do not observe multiple knickpoints in any of the channels; therefore, either (1) no linkage took place along the outlet of the channels, (2) the knickpoints formed by linkage consumed the older knickpoints, which can occur if $n > 1$ [11], or (3) the fault initiation took place in a zone of linkage (i.e., basin 14, Figure 12).

The fault at basin 1 propagates only a few kilometers southward, which serves as a plausible reason why no transience is observed in rivers south of basin 1. Other plausible reasons include the fact that different rock types such as carbonates and sandstones also exist in rivers south of basin 1, potentially modulating transient channel response. However, given the consistency in fault length and our observed displacement distribution, we prefer the model in which the fault is pinched out just south of basin 1. Overall, given the listed assumptions above, the spatial and temporal slip patterns of the Western North Boulder fault were recreated assuming a step function in base level fall and an n value of 1.

5.2. Fault Slip Rates. With an assumed normal fault geometry of 60°, we calculate a range of slip rates for each basin with initiation times from the step function in base level fall and $n = 1$ simulations (Table 5). Slip rates across all 15 basins range from 0.02 to 0.45 mm/yr (Table 5). The highest slip

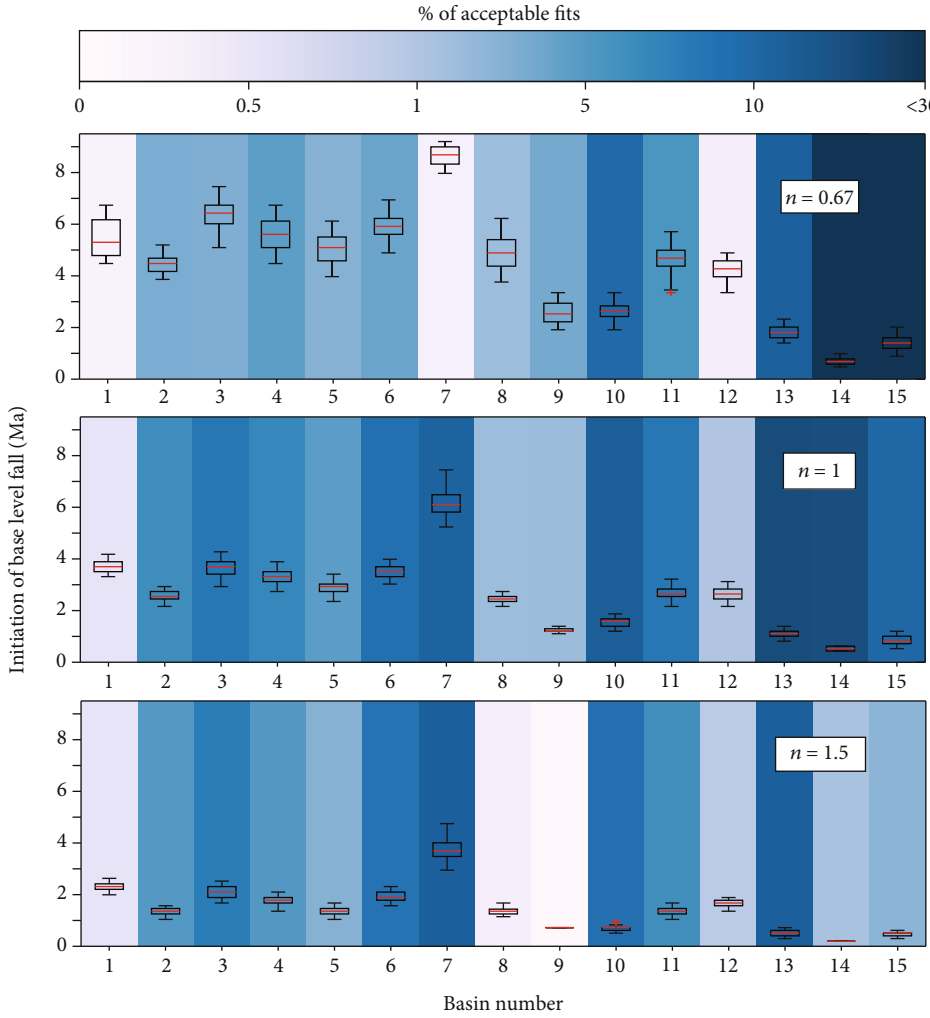

FIGURE 9: Boxplots of percent of acceptable fits for each of the model results of a step function in base level fall with n values of 0.67, 1, and 1.5. The percent of acceptable fits is representative of total simulations. The y axis represents the timing of base level fall initiation in Ma, while the x axis represents the basin number. The boxes are colored by the percent of acceptable fits for each respective basin. The red lines represent the median acceptable fit, the boxes represent the 25th and 75th percentiles, the whiskers represent nonoutliers, and the red crosses represent outliers.

rates take place along basin 14 (0.27-0.45 mm/yr), the outlet of which is assumed to be in a zone of fault linkage (Figure 12), and therefore, this is a reasonable result. Relatively high slip rates also take place along basins 8 (0.17-0.22 mm/yr) and 9 (0.32-0.41 mm/yr), which are in the central portions of the fault, a region that is anticipated to contain relatively high slip rates [9, 30]. Furthermore, all of the calculated slip rates are comparable to the USGS estimated slip rates of the Western North Boulder Fault (<0.2 mm/yr, Johns et al., 1982) and other normal faults in the region, including the Beaver Creek Fault (<0.2 mm/yr), Tobacco Root Fault (<0.2 mm/yr), Bridger Fault (<0.2 mm/yr) (U.S. Geological Survey and Montana Bureau of Mines and Geology, Quaternary fault and fold database for the United States), and the Lemhi, Lost River, and Beaverhead faults (≤0.3 mm/yr) [33], thus increasing our confidence in the results.

Our range of transient/adjusted landscape erosion rates (0.021 ± 0.002 to 0.04 ± 0.001 mm/yr) falls within the low end of the calculated slip rates (0.02 to 0.45 mm/yr). We conclude that these erosion rates may be underestimates due to the limited extent of the transient/adjusted landscape and variable lithology within the basins (e.g., presence of non-quartz yielding units such as gabbro within the transient/adjusted landscape).

5.3. Base Level Fall. Our results show that the percent of acceptable fits is significantly higher for the step function in base level fall rather than the linearly increasing rate of base level fall (Figure 8). We expect the large percent of acceptable fits for this step function in base level fall for the following reasons: (1) all channels contain a single knickpoint with a slope-break morphology (Figures 5(a) and 5(d)) that displays a consistent change in channel steepness above and below the knickpoint (Figure 1(a)), which typically develops in response to a step function in tectonic forcing [70]. (2) The consistency of adjusted channel k_{sn} values and their linearity on X-plots (Figures 5(a) and 5(d)) suggests that either the

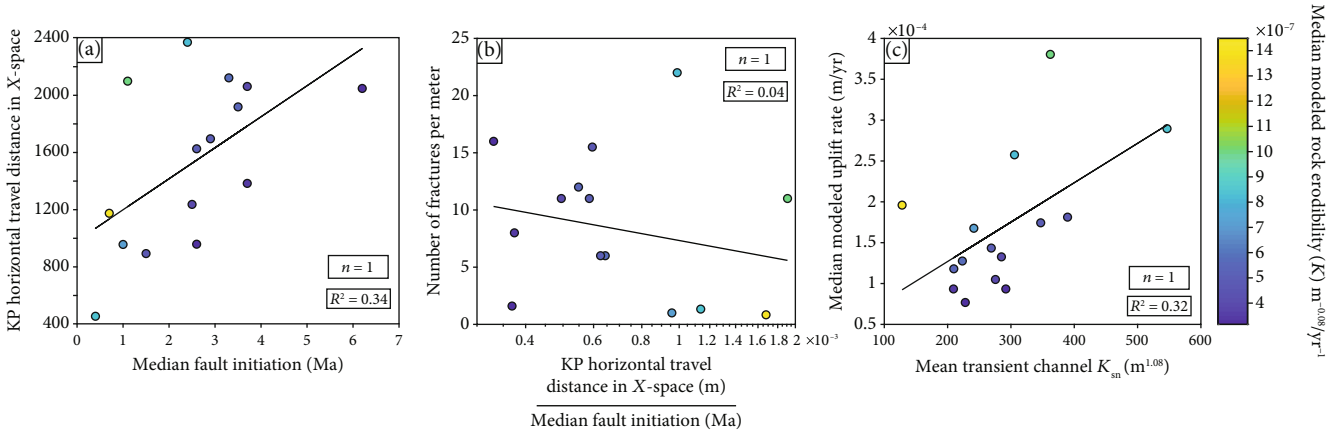

FIGURE 10: (a)–(c) Comparing stream morphology, bedrock fracture density, and stream power incision model data. (a) Knickpoint (KP) horizontal travel distances in X-space compared with the accepted median modeled fault initiation times. (b) Basin-wide median bedrock fracture density values (number of fractures every meter) compared with the knickpoint horizontal travel distances in X-space divided by their respective median fault initiation times. (c) Mean transient channel normalized steepness (k_{sn}) values compared with the median modeled uplift rate values for the median initiation of base level fall for each basin. All modeled data shown is from a simulated step function in base level fall with a slope exponent (n) value of 1.

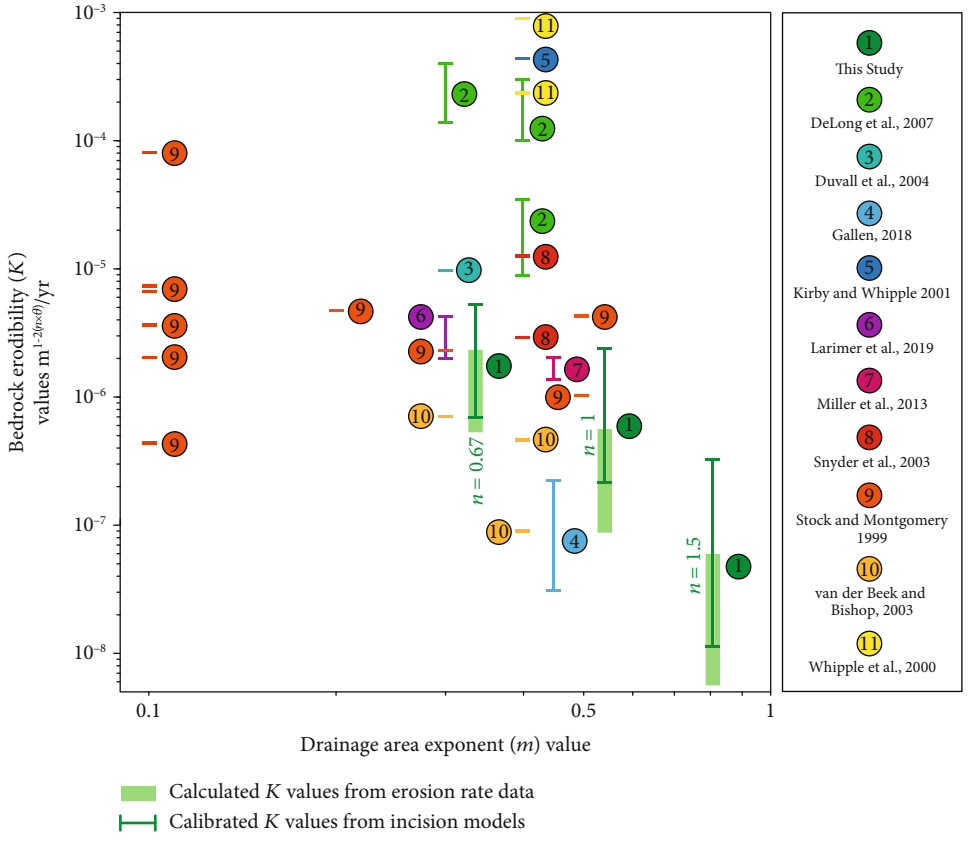

FIGURE 11: (a)–(c) Comparing the best fit calibrated bedrock erodibility (K) values to those calculated from the cosmogenic erosion rates using equation (10) and calibrated stream power K values reported in other studies ([62, 103]; Gallen, 2018; [10, 19, 67, 89–91, 104]). Our displayed range of calibrated K values (represented as solid lines) is from the simulations with a step function in base level fall with slope exponent (n) values of 0.67, 1, and 1.5. Our displayed range of K values calculated using the cosmogenic erosion rates (represented as solid bars) is also calculated with n values of 0.67, 1, and 1.5. The y axis represents calibrated bedrock erodibility (K) values, colored and numbered by their respective study. The x axis represents the drainage area exponent (m) value used within each studies' K calibration.

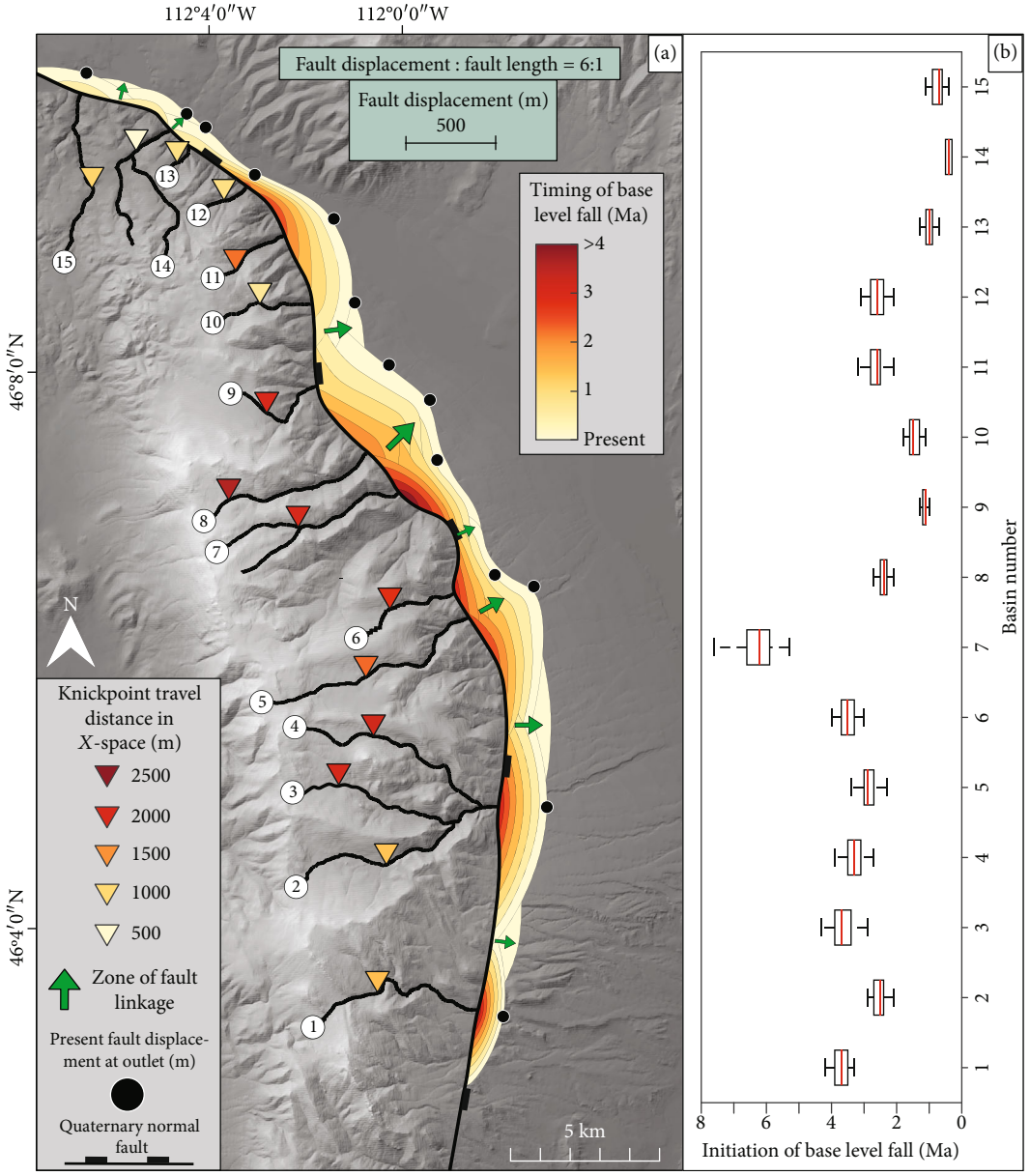

FIGURE 12: (a, b) Reconstruction of the evolution of the Western North Boulder Fault through time. The fault evolution was reconstructed using the median acceptable time values for the $n = 1$ step function base level fall model results displayed in Figure 5(b). Fault displacement values were calculated using transient channel incision depths and an assumed normal fault angle of 60°. The length of each fault segment was calculated using the fault scaling parameter described in equation (12). The fault displacement-length contours are colored by their respective age. The triangles represent the knickpoint locations, colored by their horizontal travel distances in X-space. The green arrows represent zones of fault linkage. The size of the arrows holds no significance and only change for visual clarity. The black dots represent the present fault displacement values at the outlet of each basin. For visual clarity, the fault displacement to length values are scaled 6 : 1.

rate of base level fall is near constant (i.e., step function) from its initiation to the present [11] or it is hidden by our reference concavity and assumption of spatially uniform uplift. (3) All 15 knickpoints do not correlate with a specific rock type (Figures 5(d) and 7), suggesting that knickpoint formation is not attributed to lithology. Therefore, we attribute the most probable formation of the slope-break knickpoints and pattern of k_{sn} values in the transient and relict reaches to a two-phase base level fall history along Western North Boulder Fault, where the relict reaches are representative of the relatively low, old rate of base level fall, while the transient reaches are adjusting to the step function of a relatively faster rate of base level fall (Figures 1(a) and 1(b)). We acknowledge that there could be temporal variations in base level fall; however, any such variability is likely less than the difference between the modern and relict base level fall and is not resolvable with our river profile reconstruction approach.

5.4. Along Strike Patterns of Uplift, Erosion, and River Morphology. The relationships among knickpoint horizontal

Table 5: Estimated fault slip rates.

Basin	Total fault slip (m)	Initiation time (Ma)	Fault slip rate (mm/yr)
1	144	3.3-4.2	0.03-0.04
2	211	2.1-2.9	0.07-0.1
3	273	2.9-4.3	0.06-0.09
4	305	2.7-3.9	0.08-0.11
5	397	2.3-3.4	0.12-0.17
6	239	3.0-4.0	0.06-0.08
7	266	5.3-7.6	0.03-0.05
8	462	2.1-2.7	0.17-0.22
9	410	1.0-1.3	0.32-0.41
10	234	1.1-1.8	0.13-0.21
11	284	2.1-3.2	0.09-0.14
12	68	2.1-3.1	0.02-0.03
13	127	0.7-1.3	0.10-0.18
14	134	0.3-0.5	0.27-0.45
15	115	0.4-1.1	0.10-0.29

travel distance in X-space, initiation of base level fall, and bedrock properties (Figures 10(a)–10(c); Table 1) warrant some discussion. Specifically, knickpoint horizontal travel distance in X-space and initiation of base level fall have a weak correlation (Figure 10(a)); however, there is some variation from this trend (i.e., basins 7, 8, and 9). Deviation from this correlation is reasonable, as studies have shown that even after knickpoints are normalized for the drainage area, there is a trend for higher knickpoint retreat rates with higher slip rates, which may be driven by dynamic channel narrowing effects [9, 14, 23, 95–97, 111].

In the simulations using a step function in base level fall and an n value of 1, our constrained bedrock erodibility (K) values range between $\sim 2.2 \times 10 - 7$ to $2.4 \times 10^{-6}\ \mathrm{m}^{-0.08}/\mathrm{yr}$ (Figure 11). These values have a strong pattern of increasing with the normalized knickpoint horizontal travel distances (Figure 10(b)). This intuitively makes sense, as the higher the bedrock erodibility (K), the faster the knickpoint can migrate upstream [11]. If our assumptions are correct (i.e., step function change in base level fall and no dynamic channel width adjustments), then we have confidence that the modeled bedrock erodibility (K) values reflect the actual values in nature. This claim is reinforced by the fact that our constrained K values fall within range of the K values calculated from our CRN-derived erosion rates and the calibrated stream power K values reported in other studies (Figure 11).

Because the slope exponent (n) values are postulated to reflect dominant incision processes, with plucking consistent with n values of ~ 0.67 to 1 and abrasion consistent with n values of ~ 1.5 [67], the poor correlation between the knickpoint travel distances (normalized by respective fault initiation times for n =1 simulations) and respective fracture density values (Figure 10(b)) suggests that either (1) abrasion (correlated with Schmidt rebound values) is a more dominant process than plucking (correlated with fracture density), (2) the fracture density values are not truly representative of the basins, or (3) the Schmidt rebound and fracture density data collected are not sufficient enough to deduce the prominent erosional processes taking place within the channels (Figures 10(a) and 10(b)). The latter of these hypotheses is also supported by the poor correlation between mean transient channel k_{sn} values and median uplift rates (Figure 10(c)). Even with the confidence in our modeled K values, we clearly do not have a strong metric for erodibility (e.g., fracture spacing). We acknowledge that bedrock strength, fracture density, and other factors such as grain size, sediment load, bed cover, drainage area, n value, drainage capture, and drainage divide instabilities vary in space and time during transient incision, further complicating dominant erosional processes and the rate of knickpoint retreat in our study area [23, 36, 60, 62, 95, 111–114].

5.5. Caveats. There are several assumptions that are necessary to obey the fault scaling relationships in our Western North Boulder fault reconstruction. First, basin 7 has a significantly older initiation of base level fall (>2 Ma) than its neighboring basins 6 and 8 (Figure 9). To obey fault scaling relationships, we recognize that the initiation of base level fall is unreasonably older than surrounding basins due to its low modeled bedrock erodibility value, causing a slower rate of knickpoint migration and therefore an older initiation of base level fall. This low bedrock erodibility value is a result of its relatively high normalized steepness value, which may be due to drainage capture from surrounding basins. This is suggested by the differences in shape and size of neighboring basins (Figures 1(a) and 1(b) and 5(a)) [58]. If we assume that its fault initiation is similar to neighboring basins 6 and 8, we reconstruct more realistic fault scaling relationships. Secondly, basins 2, 3, and 4 all share the same outlet, yet vary in the initiation of base level fall due to differences in knickpoint horizontal travel distances, elevations, and transient channel incision depths (Figures 5(a)–5(d)). These differences in knickpoint metrics could be due to drainage capture or lithological variations (Figure 7). While we acknowledge variability exists from basin to basin, the general trend of fault slip and initiation follows expectations from the fault slip distribution and timing in the Northern Basin and Range province and Southwest Montana.

Furthermore, we acknowledge that the cosmogenic erosion rate data only integrates over ~ 10 k.y. but the landscape has been evolving over millions of years. If the cosmogenic erosion rate data underestimates the true long-term erosion rates, bedrock erodibility values would be larger and therefore, the modeled initiations of base level fall would be younger. Conversely, an overestimate of long-term erosion rates would cause the modeled initiation of the base level to be older. Nonetheless, the general pattern of initiation times would be the same.

The erosion rate values also contain considerable error due to the limited extent of the transient/adjusted landscape and varying lithologies and therefore quartz concentrations within the basins. This is most clearly seen in basin 4, where the granite-dominated relict landscape contains a higher quartz concentration and erosion rate than the quartz-

depleted downstream transient landscape of gabbro and diorite. Here, it is likely that most of the quartz within the transient landscape were shed from the relict landscape, and therefore, the corresponding erosion rates are not truly reflective of their surrounding topography. This source of error applies to all basins with variable lithology and limited extent of the transient/adjusted landscape.

While absolute values of the fault reconstruction in Figure 12 have uncertainty, we are confident that the general pattern is robust. Moreover, we provide the first quantitative constraints on fault initiation and evolution of the Western North Boulder fault; perhaps, the farthest north basin in the Northern Basin and Range province that such constraints exist. We illustrate the utility of river profile analysis in documenting normal fault evolution, especially in young systems where slip rates and total throw are too low to extract via other geologic methods.

6. Conclusions

The eastern margin of Bull Mountain in the Northern Basin and Range province contains a steep, dissected transient landscape that is most likely attributed to the recent base level fall of the Western North Boulder fault. We show that transient channel morphometrics, rock strength metrics, cosmogenic erosion rates, and calibrated stream power incision models can constrain the temporal and spatial patterns of base level fall along the Western North Boulder fault. We show that with a step function in base level fall and an n value of 1, the Western North Boulder fault started as individual fault segments along the middle to southern regions of Bull Mountain that nucleated around 6.2 to 2.5 Ma, respectively. This was followed by the nucleation of other fault segments in the northern region around 1.5 to 0.4 Ma. Through time, these faults linked together to span over 40 km, with a maximum fault slip of 462 m (basin 8) in the central portion of the fault. Fault slip rates range from 0.02 to 0.45 mm/yr along strike and are similar to estimates for other faults in the region.

Our results augment existing constraints of Quaternary fault slip histories in the Northern Basin and Range province. We find that the timing of fault initiation coincides well with the migration of the Yellowstone hotspot across the Idaho-Montana border. Therefore, we confidently attribute the increased extension along the Western North Boulder fault to the crustal bulge from the migrating hotspot. However, the base level fall simulations show that the slope exponent (n) value can significantly change the estimated timing of fault initiation required to match observed knickpoint locations, highlighting the importance of this parameter when using the stream power equation. Furthermore, our range of calibrated bedrock erodibility (K) values are comparable to those calculated from the cosmogenic erosion rates and calibrated stream power K values reported in other studies, increasing confidence in our results. Overall, we show that rivers are powerful tools for documenting the spatial and temporal patterns of normal fault evolution, especially where other geologic/geodetic methods are limited, proving to be a vital tool for accurate tectonic hazard assessments.

Data Availability

This study's data are available in the IUScholarWorks digital repository at Indiana University (http://hdl.handle.net/2022/25807).

Conflicts of Interest

The authors declare no conflict of interest regarding this publication.

Acknowledgments

This work has been conducted with financial support from the National Science Foundation grants 4827341 and 1727139, the Army Research Laboratory grant W911NF-17-1-0248, the Geological Society of America Robert K. Fahnestock grant, the Indiana University Field Station Vitaliano grant, Indiana University Graduate and Professional Student Government, and the Indiana University Department of Earth and Atmospheric sciences. Yanites and Mitchell was supported by the National Science Foundation grant EAR-1727139. A large portion of data in this study was collected on the properties of the Carey, Dawson, and McCauley families, Ms. Norby, Ms. Warthen, and Dr. Pontiac. Cosmogenic nuclide concentrations were measured at the Purdue University PRIME laboratory. This work greatly benefited from thoughtful reviews by Sean Gallen, Sarah Boulton, and an anonymous reviewer; however, any errors or inaccuracies presented here are solely the responsibility of the authors.

Supplementary Materials

The attached supplementary material file contains 14 figures displaying calibrated stream power incision model results using different uplift rates through time, a guide to our interpretive reconstruction of the Western North Boulder fault evolution, and field photos showing some examples of the relict and transient reaches in the studied basins. Figure descriptions are located below each respective figure. *(Supplementary Materials)*

References

[1] K. X. Whipple and G. E. Tucker, "Dynamics of the stream-power river incision model: implications for height limits of mountain ranges, landscape response timescales, and research needs," *Journal of Geophysical Research: Solid Earth*, vol. 104, no. B8, pp. 17661–17674, 1999.

[2] A. M. Forte, B. J. Yanites, and K. X. Whipple, "Complexities of landscape evolution during incision through layered stratigraphy with contrasts in rock strength," *Earth Surface Processes and Landforms*, vol. 41, no. 12, pp. 1736–1757, 2016.

[3] L. S. Sklar and W. E. Dietrich, "Sediment and rock strength controls on river incision into bedrock," *Geology*, vol. 29, no. 12, pp. 1087–1090, 2001.

[4] A. C. Whittaker, "How do landscapes record tectonics and climate?," *Lithosphere*, vol. 4, no. 2, pp. 160–164, 2012.

[5] M. A. Ellis, J. B. Barnes, and J. P. Colgan, "Geomorphic evidence for enhanced Pliocene–quaternary faulting in the northwestern Basin and Range," *Lithosphere*, vol. 7, no. 1, pp. 59–72, 2015.

[6] S. F. Gallen, K. W. Wegmann, and D. R. Bohnenstieh, "Miocene rejuvenation of topographic relief in the southern Appalachians," *GSA Today*, vol. 23, no. 2, pp. 4–10, 2013.

[7] N. M. Gasparini and K. X. Whipple, "Diagnosing climatic and tectonic controls on topography: eastern flank of the northern Bolivian Andes," *Lithosphere*, vol. 6, no. 4, pp. 230–250, 2014.

[8] L. Goren, M. Fox, and S. D. Willett, "Tectonics from fluvial topography using formal linear inversion: theory and applications to the Inyo Mountains, California," *Journal of Geophysical Research: Earth Surface*, vol. 119, no. 8, pp. 1651–1681, 2014.

[9] E. Kent, S. J. Boulton, A. C. Whittaker, I. S. Stewart, and M. Cihat Alçiçek, "Normal fault growth and linkage in the Gediz (Alaşehir) Graben, Western Turkey, revealed by transient river long-profiles and slope-break knickpoints," *Earth Surface Processes and Landforms*, vol. 42, no. 5, pp. 836–852, 2017.

[10] J. E. Larimer, B. J. Yanites, W. Phillips, and E. Mittelstaedt, "Late Miocene rejuvenation of Central Idaho landscape evolution: a case for surface processes driven by plume-lithosphere interaction," *Lithosphere*, vol. 11, pp. 59–72, 2019.

[11] N. A. Mitchell and B. J. Yanites, "Spatially variable increase in rock uplift in the northern U.S. Cordillera recorded in the distribution of river Knickpoints and incision Depths," *Journal of Geophysical Research: Earth Surface*, vol. 124, no. 5, pp. 1238–1260, 2019.

[12] F. Pavano, F. J. Pazzaglia, and S. Catalano, "Knickpoints as geomorphic markers of active tectonics: a case study from northeastern Sicily (southern Italy)," *Lithosphere*, vol. 8, no. 6, pp. 633–648, 2016.

[13] N. P. Snyder, K. X. Whipple, G. E. Tucker, and D. J. Merritts, "Landscape response to tectonic forcing: digital elevation model analysis of stream profiles in the Mendocino triple junction region, northern California," *Geological Society of America Bulletin*, vol. 112, no. 8, pp. 1250–1263, 2000.

[14] A. C. Whittaker and S. J. Boulton, "Tectonic and climatic controls on knickpoint retreat rates and landscape response times," *Journal of Geophysical Research - Earth Surface*, vol. 117, no. F2, 2012.

[15] C. Wobus, K. X. Whipple, E. Kirby et al., "Tectonics from topography: procedures, promise, and pitfalls," in *Tectonics, Climate, and Landscape Evolution*, S. D. Willett, N. Hovius, M. T. Brandon, and D. M. Fisher, Eds., Geological Society of America, 2006.

[16] S. J. Boulton and A. C. Whittaker, "Quantifying the slip rates, spatial distribution and evolution of active normal faults from geomorphic analysis: field examples from an oblique-extensional graben, southern Turkey," *Geomorphology*, vol. 104, no. 3-4, pp. 299–316, 2009.

[17] S. F. Gallen and K. W. Wegmann, "River profile response to normal fault growth and linkage: an example from the Hellenic forearc of south-Central Crete, Greece," *Earth Surface Dynamics*, vol. 5, no. 1, pp. 161–186, 2017.

[18] A. J. Cyr, D. E. Granger, V. Olivetti, and P. Molin, "Quantifying rock uplift rates using channel steepness and cosmogenic nuclide–determined erosion rates: examples from northern and southern Italy," *Lithosphere*, vol. 2, no. 3, pp. 188–198, 2010.

[19] E. Kirby and K. Whipple, "Quantifying differential rock-uplift rates via stream profile analysis," *Geology*, vol. 29, no. 5, pp. 415–418, 2001.

[20] S. R. Miller, S. L. Baldwin, and P. G. Fitzgerald, "Transient fluvial incision and active surface uplift in the Woodlark Rift of eastern Papua New Guinea," *Lithosphere*, vol. 4, no. 2, pp. 131–149, 2012.

[21] L. Royden and J. Taylor Perron, "Solutions of the stream power equation and application to the evolution of river longitudinal profiles," *Journal of Geophysical Research - Earth Surface*, vol. 118, no. 2, pp. 497–518, 2013.

[22] K. X. Whipple, "Bedrock rivers and the geomorphology of active orogens," *Annual Review of Earth and Planetary Sciences*, vol. 32, no. 1, pp. 151–185, 2004.

[23] A. C. Whittaker, P. A. Cowie, M. Attal, G. E. Tucker, and G. P. Roberts, "Bedrock channel adjustment to tectonic forcing: implications for predicting river incision rates," *Geology*, vol. 35, no. 2, p. 103, 2007.

[24] B. J. Yanites, G. E. Tucker, K. J. Mueller, and Y.-G. Chen, "How rivers react to large earthquakes: evidence from Central Taiwan," *Geology*, vol. 38, no. 7, pp. 639–642, 2010.

[25] P. W. Reiners and M. T. Brandon, "Using THERMOCHRONOLOGY to understand OROGENIC erosion," *Annual Review of Earth and Planetary Sciences*, vol. 34, no. 1, pp. 419–466, 2006.

[26] T. H. Dixon, E. Norabuena, and L. Hotaling, "Paleoseismology and global positioning system: earthquake-cycle effects and geodetic versus geologic fault slip rates in the eastern California shear zone," *Geology*, vol. 31, no. 1, pp. 55–58, 2003.

[27] M. M. Berlin and R. S. Anderson, "Steepened channels upstream of knickpoints: Controls on relict landscape response," *Journal of Geophysical Research: Earth Surface*, vol. 114, no. F3, p. 114, 2009.

[28] B. T. Crosby and K. X. Whipple, "Knickpoint initiation and distribution within fluvial networks: 236 waterfalls in the Waipaoa River, North Island, New Zealand," *Geomorphology, The Hydrology and Geomorphology of Bedrock Rivers*, vol. 82, no. 1-2, pp. 16–38, 2006.

[29] N. A. Rosenbloom and R. S. Anderson, "Hillslope and channel evolution in a marine terraced landscape, Santa Cruz, California," *Journal of Geophysical Research: Solid Earth*, vol. 99, no. B7, pp. 14013–14029, 1994.

[30] P. A. Cowie and G. P. Roberts, "Constraining slip rates and spacings for active normal faults," *Journal of Structural Geology*, vol. 23, no. 12, pp. 1901–1915, 2001.

[31] M. A. E. Curry, J. B. Barnes, and J. P. Colgan, "Testing fault growth models with low-temperature thermochronology in the northwest Basin and Range, USA," *Tectonics*, vol. 35, no. 10, pp. 2467–2492, 2016.

[32] N. H. Dawers and M. H. Anders, "Displacement-length scaling and fault linkage," *Journal of Structural Geology*, vol. 17, no. 5, pp. 607–614, 1995.

[33] A. L. Densmore, S. Gupta, P. A. Allen, and N. H. Dawers, "Transient landscapes at fault tips," *Journal of Geophysical Research - Earth Surface*, vol. 112, no. F3, 2007.

[34] E. Kent, S. J. Boulton, I. S. Stewart, A. C. Whittaker, and M. C. Alçiçek, "Geomorphic and geological constraints on the active normal faulting of the Gediz (Alaşehir) Graben,

Western Turkey," *Journal of the Geological Society*, vol. 173, no. 4, pp. 666–678, 2016.

[35] R. W. Schlische, S. S. Young, R. V. Ackermann, and A. Gupta, "Geometry and scaling relations of a population of very small rift-related normal faults," *Geology*, vol. 24, no. 8, pp. 683–686, 1996.

[36] G. E. Tucker and K. X. Whipple, "Topographic outcomes predicted by stream erosion models: Sensitivity analysis and intermodel comparison," *Journal of Geophysical Research: Solid Earth*, vol. 107, 2002.

[37] P. G. DeCelles, "Late Jurassic to Eocene evolution of the Cordilleran thrust belt and foreland basin system, western U.S.A," *American Journal of Science*, vol. 304, no. 2, pp. 105–168, 2004.

[38] T. M. Schwartz and R. K. Schwartz, "Paleogene postcompressional intermontane basin evolution along the frontal cordilleran fold-and-thrust belt of southwestern Montana," *Geological Society of America Bulletin*, vol. 125, no. 5-6, pp. 961–984, 2013.

[39] T. J. Kalakay, B. E. John, and D. R. Lageson, "Fault-controlled pluton emplacement in the Sevier fold-and-thrust belt of southwest Montana, USA," *Journal of Structural Geology*, vol. 23, no. 6-7, pp. 1151–1165, 2001.

[40] W. Fritz, J. Sears, R. McDowell, and J. Wampler, "Cenozoic volcanic rocks of southwestern Montana," *Northwestern Geology*, vol. 36, pp. 91–110, 2007.

[41] D. R. Lageson, J. G. Schmitt, B. K. Horton, T. J. Kalakay, and B. R. Burton, "Influence of Late Cretaceous magmatism on the Sevier orogenic wedge, western Montana," *Geology*, vol. 29, no. 8, pp. 723–726, 2001.

[42] F. Ö. Dudás, V. O. Ispolatov, S. S. Harlan, and L. W. Snee, "40Ar/39Ar geochronology and geochemical reconnaissance of the Eocene Lowland Creek Volcanic Field, West-Central Montana," *Journal of Geology*, vol. 118, no. 3, pp. 295–304, 2010.

[43] K. Lund, J. N. Aleinikoff, M. J. Kunk et al., "SHRIMP U-Pb and 40Ar/39Ar age constraints for relating plutonism and mineralization in the boulder batholith Region, Montana," *Economic Geology*, vol. 97, no. 2, pp. 241–267, 2002.

[44] G. D. Robinson, M. R. Klepper, and J. D. Obradovich, "Overlapping plutonism, volcanism, and tectonism in the boulder batholith region, western Montana," *Memoir - Geological Society of America*, vol. 116, 1968.

[45] E. H. Bennett, "Relationship of the trans-challis fault system in Central Idaho to Eocene and basin and range extensions," *Geology*, vol. 14, no. 6, pp. 481–484, 1986.

[46] V. E. Camp, K. L. Pierce, and L. A. Morgan, "Yellowstone plume trigger for basin and range extension, and coeval emplacement of the Nevada–Columbia Basin magmatic belt," *Geosphere*, vol. 11, no. 2, pp. 203–225, 2015.

[47] K. N. Constenius, "Late Paleogene extensional collapse of the Cordilleran foreland fold and thrust belt," *Geological Society of America Bulletin*, vol. 20, 1996.

[48] S. U. Janecke, "Kinematics and timing of three superposed extensional systems, east Central Idaho: evidence for an Eocene tectonic transition," *Tectonics*, vol. 11, no. 6, pp. 1121–1138, 1992.

[49] S. U. Janecke, C. J. Vandenburg, and J. J. Blankenau, "Geometry, mechanisms and significance of extensional folds from examples in the Rocky Mountain Basin and Range province, U.S.a," *Journal of Structural Geology*, vol. 20, no. 7, pp. 841–856, 1998.

[50] L. J. Sonder and C. H. Jones, "Western United States extension: how the west was widened," *Annual Review of Earth and Planetary Sciences*, vol. 27, no. 1, pp. 417–462, 1999.

[51] M. H. Anders, J. W. Geissman, L. A. Piety, and J. T. Sullivan, "Parabolic distribution of circumeastern Snake River plain seismicity and latest quaternary faulting: migratory pattern and association with the Yellowstone hotspot," *Journal of Geophysical Research: Solid Earth*, vol. 94, no. B2, pp. 1589–1621, 1989.

[52] W. J. Fritz and J. W. Sears, "Tectonics of the Yellowstone hotspot wake in, southwestern Montana," *Geology*, vol. 21, no. 5, article 10.1130/0091-7613(1993)021<0427:TOTYHW>2.3.CO;2, pp. 427–430, 1993.

[53] S. Janecke, "Cenozoic Extensional Processes and Tectonics in the Northern Rocky Mountains: Southwest Montana and Eastern Idaho," *Northwest Geology*, vol. 36, pp. 111–132, 2007.

[54] K. Pierce and L. Morgan, "Chapter 1: the track of the Yellowstone hot spot: volcanism, faulting, and uplift," in *Memoir*, pp. 1–54, Geological Society of America, 1992.

[55] K. L. Pierce and L. A. Morgan, "Is the track of the Yellowstone hotspot driven by a deep mantle plume? — review of volcanism, faulting, and uplift in light of new data," *Journal of Volcanology and Geothermal Research*, vol. 188, no. 1-3, pp. 1–25, 2009.

[56] A. L. Densmore, R. Hetzel, S. Ivy-Ochs, W. C. Krugh, N. Dawers, and P. Kubik, "Spatial variations in catchment-averaged denudation rates from normal fault footwalls," *Geology*, vol. 37, no. 12, pp. 1139–1142, 2009.

[57] N. W. Harkins, D. J. Anastasio, and F. J. Pazzaglia, "Tectonic geomorphology of the red rock fault, insights into segmentation and landscape evolution of a developing range front normal fault," *Journal of Structural Geology*, vol. 27, no. 11, pp. 1925–1939, 2005.

[58] S. D. Willett, S. W. McCoy, J. T. Perron, L. Goren, and C.-Y. Chen, "Dynamic reorganization of river basins," *Science*, vol. 343, no. 6175, p. 1248765, 2014.

[59] B. J. Yanites, T. A. Ehlers, J. K. Becker, M. Schnellmann, and S. Heuberger, "High magnitude and rapid incision from river capture: Rhine River, Switzerland," *Journal of Geophysical Research: Earth Surface*, vol. 118, no. 2, pp. 1060–1084, 2013.

[60] N. Bursztyn, J. L. Pederson, C. Tressler, R. D. Mackley, and K. J. Mitchell, "Rock strength along a fluvial transect of the Colorado Plateau – quantifying a fundamental control on geomorphology," *Earth and Planetary Science Letters*, vol. 429, pp. 90–100, 2015.

[61] R. A. DiBiase, M. W. Rossi, and A. B. Neely, "Fracture density and grain size controls on the relief structure of bedrock landscapes," *Geology*, vol. 46, no. 5, pp. 399–402, 2018.

[62] A. Duvall, E. Kirby, and D. Burbank, "Tectonic and lithologic controls on bedrock channel profiles and processes in coastal California," *Journal of Geophysical Research - Earth Surface*, vol. 109, no. F3, 2004.

[63] S. F. Gallen, "The influence of bedrock erodibility on landscape dynamics in decay phase orogens and its implications for sedimentary systems," in *AGU Fall Meeting Abstracts*, American Geophysical Union, 2018.

[64] W. Schwanghart and N. J. Kuhn, "TopoToolbox: a set of Matlab functions for topographic analysis," *Environmental Modelling & Software*, vol. 25, no. 6, pp. 770–781, 2010.

[65] W. Schwanghart and D. Scherler, "Short Communication: TopoToolbox 2 – MATLAB-based software for topographic analysis and modeling in Earth surface sciences," *Earth Surface Dynamics*, vol. 2, no. 1, pp. 1–7, 2014.

[66] A. D. Howard, "A detachment-limited model of drainage basin evolution," *Water Resources Research*, vol. 30, no. 7, pp. 2261–2285, 1994.

[67] K. X. Whipple, G. S. Hancock, and R. S. Anderson, "River incision into bedrock: mechanics and relative efficacy of plucking, abrasion, and cavitation," *GSA Bulletin*, vol. 112, no. 3, pp. 490–503, 2000.

[68] J. J. Flint, "Stream gradient as a function of order, magnitude, and discharge," *Water Resources Research*, vol. 10, no. 5, pp. 969–973, 1974.

[69] A. D. Howard and G. Kerby, "Channel changes in badlands," *Geological Society of America Bulletin*, vol. 94, no. 6, pp. 739–752, 1983.

[70] E. Kirby and K. X. Whipple, "Expression of active tectonics in erosional landscapes," *Journal of Structural Geology*, vol. 44, pp. 54–75, 2012.

[71] N. Harkins, E. Kirby, A. Heimsath, R. Robinson, and U. Reiser, "Transient fluvial incision in the headwaters of the Yellow River, northeastern Tibet, China," *Journal of Geophysical Research: Earth Surface*, vol. 112, no. F3, 2007.

[72] E. Kirby, K. X. Whipple, W. Tang, and Z. Chen, "Distribution of active rock uplift along the eastern margin of the Tibetan plateau: inferences from bedrock channel longitudinal profiles," *Journal of Geophysical Research - Solid Earth*, vol. 108, no. B4, 2003.

[73] W. B. Ouimet, K. X. Whipple, and D. E. Granger, "Beyond threshold hillslopes: channel adjustment to base-level fall in tectonically active mountain ranges," *Geology*, vol. 37, no. 7, pp. 579–582, 2009.

[74] A. C. Whittaker, M. Attal, P. A. Cowie, G. E. Tucker, and G. Roberts, "Decoding temporal and spatial patterns of fault uplift using transient river long profiles," *Geomorphology*, vol. 100, no. 3-4, pp. 506–526, 2008.

[75] S. M. Mudd, M. Attal, D. T. Milodowski, S. W. D. Grieve, and D. A. Valters, "A statistical framework to quantify spatial variation in channel gradients using the integral method of channel profile analysis," *Journal of Geophysical Research - Earth Surface*, vol. 119, no. 2, pp. 138–152, 2014.

[76] P. England and P. Molnar, "Surface uplift, uplift of rocks, and exhumation of rocks," *Geology*, vol. 18, no. 12, pp. 1173–1177, 1990.

[77] L. M. Schoenbohm, K. X. Whipple, B. C. Burchfiel, and L. Chen, "Geomorphic constraints on surface uplift, exhumation, and plateau growth in the Red River region, Yunnan Province, China," *Geological Society of America Bulletin*, vol. 116, no. 7, p. 895, 2004.

[78] A. C. Whittaker and A. S. Walker, "Geomorphic constraints on fault throw rates and linkage times: examples from the Northern Gulf of Evia, Greece," *Journal of Geophysical Research: Earth Surface*, vol. 120, no. 1, pp. 137–158, 2015.

[79] P. Bierman and E. J. Steig, "Estimating rates of denudation using cosmogenic isotope abundances in sediment," *Earth Surface Processes and Landforms*, vol. 21, no. 2, pp. 125–139, 1996.

[80] E. T. Brown, R. F. Stallard, M. C. Larsen, G. M. Raisbeck, and F. Yiou, "Denudation rates determined from the accumulation of in situ-produced 10Be in the Luquillo experimental forest, Puerto Rico," *Earth and Planetary Science Letters*, vol. 129, no. 1-4, pp. 193–202, 1995.

[81] D. E. Granger, J. W. Kirchner, and R. Finkel, "Spatially averaged long-term erosion rates measured from in situ-produced cosmogenic nuclides in alluvial sediment," *Journal of Geology*, vol. 104, no. 3, pp. 249–257, 1996.

[82] G. M. Stock, K. L. Frankel, T. A. Ehlers, M. Schaller, S. M. Briggs, and R. C. Finkel, "Spatial and temporal variations in denudation of the Wasatch Mountains, Utah, USA," *Lithosphere*, vol. 1, no. 1, pp. 34–40, 2009.

[83] H. Wittmann, F. Blanckenburgvon, T. Kruesmann, K. P. Norton, and P. W. Kubik, "Relation between rock uplift and denudation from cosmogenic nuclides in river sediment in the Central Alps of Switzerland," *Journal of Geophysical Research - Earth Surface*, vol. 112, no. F4, 2007.

[84] B. J. Yanites, G. E. Tucker, and R. S. Anderson, "Numerical and analytical models of cosmogenic radionuclide dynamics in landslide-dominated drainage basins," *Journal of Geophysical Research*, vol. 114, no. F1, p. 114, 2009.

[85] C. P. Kohl and K. Nishiizumi, "Chemical isolation of quartz for measurement of in-situ -produced cosmogenic nuclides," *Geochimica et Cosmochimica Acta*, vol. 56, no. 9, pp. 3583–3587, 1992.

[86] S. M. Mudd, M.-A. Harel, M. D. Hurst, S. W. D. Grieve, and S. M. Marrero, "The CAIRN method: automated, reproducible calculation of catchment-averaged denudation rates from cosmogenic nuclide concentrations," *Earth Surface Dynamics*, vol. 4, no. 3, pp. 655–674, 2016.

[87] S. F. Gallen, "Lithologic controls on landscape dynamics and aquatic species evolution in post-orogenic mountains," *Earth and Planetary Science Letters*, vol. 493, pp. 150–160, 2018.

[88] G. S. Hancock, R. S. Anderson, and K. X. Whipple, "Beyond Power: Bedrock River Incision Process and Form," in *Rivers over rock: fluvial processes in bedrock channels*, K. J. Tinkler and E. E. Wohl, Eds., pp. 35–60, American Geophysical Union, 1998.

[89] N. P. Snyder, K. X. Whipple, G. E. Tucker, and D. J. Merritts, "Channel response to tectonic forcing: field analysis of stream morphology and hydrology in the Mendocino triple junction region, northern California," *Geomorphology*, vol. 53, no. 1-2, pp. 97–127, 2003.

[90] J. D. Stock and D. R. Montgomery, "Geologic constraints on bedrock river incision using the stream power law," *Journal of Geophysical Research: Solid Earth*, vol. 104, pp. 4983–4993, 1999.

[91] P. van der Beek and P. Bishop, "Cenozoic river profile development in the Upper Lachlan catchment (SE Australia) as a test of quantitative fluvial incision models," *Journal of Geophysical Research - Solid Earth*, vol. 108, no. B6, p. 2309, 2003.

[92] M. L. Jeffery, T. A. Ehlers, B. J. Yanites, and C. J. Poulsen, "Quantifying the role of paleoclimate and Andean Plateau uplift on river incision," *Journal of Geophysical Research - Earth Surface*, vol. 118, no. 2, pp. 852–871, 2013.

[93] W. C. Haneberg, "Effects of digital elevation model errors on spatially distributed seismic slope stability calculations: an example from Seattle, Washington," *Environmental and Engineering Geoscience*, vol. 12, no. 3, pp. 247–260, 2006.

[94] J. D. Niemann, N. M. Gasparini, G. E. Tucker, and R. L. Bras, "A quantitative evaluation of Playfair's law and its use in testing long-term stream erosion models," *Earth Surface Processes and Landforms*, vol. 26, no. 12, pp. 1317–1332, 2001.

[95] N. J. Finnegan, G. Roe, D. R. Montgomery, and B. Hallet, "Controls on the channel width of rivers: implications for modeling fluvial incision of bedrock," *Geology*, vol. 33, no. 3, pp. 229–232, 2005.

[96] J. M. Turowski, D. Lague, and N. Hovius, "Response of bedrock channel width to tectonic forcing: insights from a numerical model, theoretical considerations, and comparison with field data," *Journal of Geophysical Research*, vol. 114, no. F3, 2009.

[97] B. J. Yanites, "The dynamics of channel slope, width, and sediment in actively eroding bedrock river systems," *Journal of Geophysical Research - Earth Surface*, vol. 123, no. 7, pp. 1504–1527, 2018.

[98] B. J. Yanites, G. E. Tucker, K. J. Mueller et al., "Incision and channel morphology across active structures along the Peikang River, Central Taiwan: implications for the importance of channel width," *Geological Society of America Bulletin*, vol. 122, no. 7-8, pp. 1192–1208, 2010.

[99] P. Bishop, T. B. Hoey, J. D. Jansen, and I. L. Artza, "Knickpoint recession rate and catchment area: the case of uplifted rivers in eastern Scotland," *Earth Surface Processes and Landforms*, vol. 30, no. 6, pp. 767–778, 2005.

[100] S. J. Boulton, M. Stokes, and A. E. Mather, "Transient fluvial incision as an indicator of active faulting and Plio-quaternary uplift of the Moroccan High Atlas," *Tectonophysics*, vol. 633, pp. 16–33, 2014.

[101] J. K. Willenbring, N. M. Gasparini, B. T. Crosby, and G. Brocard, "What does a mean mean? The temporal evolution of detrital cosmogenic denudation rates in a transient landscape," *Geology*, vol. 41, no. 12, pp. 1215–1218, 2013.

[102] A. M. Forte and K. X. Whipple, "Criteria and tools for determining drainage divide stability," *Earth and Planetary Science Letters*, vol. 493, pp. 102–117, 2018.

[103] S. B. DeLong, J. D. Pelletier, and L. Arnold, "Bedrock landscape development modeling: calibration using field study, geochronology, and digital elevation model analysis," *Geological Society of America Bulletin*, vol. 119, no. 1-2, pp. 157–173, 2007.

[104] S. R. Miller, P. B. Sak, E. Kirby, and P. R. Bierman, "Neogene rejuvenation of central Appalachian topography: evidence for differential rock uplift from stream profiles and erosion rates," *Earth and Planetary Science Letters*, vol. 369-370, pp. 1–12, 2013.

[105] N. B. Ciftci and E. Bozkurt, "Anomalous stress field and active breaching at relay ramps: a field example from Gediz Graben, SW Turkey," *Geological Magazine*, vol. 144, no. 4, pp. 687–699, 2007.

[106] N. H. Dawers, M. H. Anders, and C. H. Scholz, "Growth of normal faults: displacement-length scaling," *Geology*, vol. 21, no. 12, pp. 1107–1110, 1993.

[107] J. A. Cartwright, B. D. Trudgill, and C. S. Mansfield, "Fault growth by segment linkage: an explanation for scatter in maximum displacement and trace length data from the Canyonlands Grabens of SE Utah," *Journal of Structural Geology*, vol. 17, no. 9, pp. 1319–1326, 1995.

[108] A. Gupta and C. H. Scholz, "A model of normal fault interaction based on observations and theory," *Journal of Structural Geology*, vol. 22, no. 7, pp. 865–879, 2000.

[109] D. C. P. Peacock and D. J. Sanderson, "Displacements, segment linkage and relay ramps in normal fault zones," *Journal of Structural Geology*, vol. 13, no. 6, pp. 721–733, 1991.

[110] E. J. M. Willemse, D. D. Pollard, and A. Aydin, "Three-dimensional analyses of slip distributions on normal fault arrays with consequences for fault scaling," *Journal of Structural Geology*, vol. 18, no. 2-3, pp. 295–309, 1996.

[111] B. J. Yanites and G. E. Tucker, "Controls and limits on bedrock channel geometry," *Journal of Geophysical Research*, vol. 115, 2010.

[112] A. D. Howard, "Long profile development of bedrock channels: interaction of weathering, mass wasting, bed erosion, and sediment transport," in *Rivers over rock: Fluvial Process in bedrock channels*, Geophysical Monograph Series, pp. 297–319, American Geophysical Union, 1998.

[113] J. P. L. Johnson, K. X. Whipple, L. S. Sklar, and T. C. Hanks, "Transport slopes, sediment cover, and bedrock channel incision in the Henry Mountains, Utah," *Journal of Geophysical Research*, vol. 114, no. F2, 2009.

[114] L. S. Sklar and W. E. Dietrich, "The role of sediment in controlling steady-state bedrock channel slope: implications of the saltation–abrasion incision model," *Geomorphology*, vol. 82, no. 1-2, pp. 58–83, 2006.

[115] R. Braucher, P. Del Castillo, L. Siame, A. J. Hidy, and D. L. Bourlés, "Determination of both exposure time and denudation rate from an in situ-produced ^{10}Be depth profile: A mathematical proof of uniqueness. Model sensitivity and applications to natural cases," *Quaternary Geochronology*, vol. 4, pp. 56–67, 2009.